

Anatomy of parameter-estimation biases in overlapping gravitational-wave signals

Ziming Wang^{1,2}, Dicong Liang², Junjie Zhao^{3,4}, Chang Liu^{1,2,5},
Lijing Shao^{2,6}

¹ Department of Astronomy, School of Physics, Peking University, Beijing 100871, China

² Kavli Institute for Astronomy and Astrophysics, Peking University, Beijing 100871, China

³ Institute for Frontiers in Astronomy and Astrophysics, Beijing Normal University, Beijing 102206, China

⁴ Department of Astronomy, Beijing Normal University, Beijing 100875, China

⁵ Laboratoire des 2 Infinis - Toulouse (L2IT-IN2P3), Université de Toulouse, CNRS, UPS, F-31062 Toulouse Cedex 9, France

⁶ National Astronomical Observatories, Chinese Academy of Sciences, Beijing 100012, China

E-mail: lshao@pku.edu.cn (LS)

Abstract. In future gravitational-wave (GW) detections, a large number of overlapping GW signals will appear in the data stream of detectors. When extracting information from one signal, the presence of other signals can cause large parameter estimation biases. Using the Fisher matrix (FM), we develop a bias analysis procedure to investigate how each parameter of other signals affects the inference biases. Taking two-signal overlapping as an example, we show detailedly and quantitatively that the biases essentially originate from the overlapping of the frequency evolution. Furthermore, we find that the behaviors of the correlation coefficients between the parameters of the two signals are similar to the biases. Both of them can be used as characterization of the influence between signals. We also corroborate the bias results of the FM method with full Bayesian analysis. Our results can provide guidance for the development of new PE algorithms on overlapping signals, and the analysis methodology has the potential to generalize.

1. Introduction

Since the first gravitational-wave (GW) event was detected in 2015 [2], nowadays GW observatories LIGO, Virgo, and KAGRA have detected nearly 90 GW events, which greatly enhanced our understanding of fundamental physics, astrophysics, and cosmology [1, 3, 4]. In the future, the next-generation (XG) ground-based GW detectors, such as Cosmic Explorer (CE) [36, 37] and Einstein Telescope (ET) [21, 41] will be constructed. Compared with the present GW detectors, XG detectors improve the sensitivity by an order of magnitude, and have a lower cut-off frequency [28], which leads to more detectable GW events with longer signal duration. Therefore, in the data stream of XG detectors, there will be a large number of overlapping signals (OSs) [35, 40, 34, 38, 22]. For space-based GW detectors, such as Laser Interferometer Space Antenna (LISA) [5], Taiji [24] and TianQin [32, 20], a large number of OSs will also be present [6].

Searching for GW signals from detector data and extracting information of GW sources are the basis for GW science. The impact of OSs is mainly reflected in two aspects. On the one hand, every OS comes from the superposition of several independent signals, so the dimension of the parameter space is high. Conducting parameter estimation (PE) on the whole OS requires considerable computational time and resources. On the other hand, if one deals with every single signal in the OS one by one, the existence of other signals will have an impact on the PE of the target, usually reflecting as a systematic error, or the PE bias more quantitatively. Janquart *et al.* [27] referred to these two PE cases as the joint PE (JPE) and the single PE (SPE) respectively. If the SPE bias of each signal is small, then we do not need to conduct complex JPE. On the contrary, when the number of GW events is known, JPE is a better choice when SPE biases are large. Compared to JPE, computing SPE is faster, and the results of SPE can tell us whether we need JPE. Therefore, as the basis of studying the whole PE technology of OS, it is necessary and useful to investigate the behaviors of SPE first.

A number of publications [35, 40, 34, 38, 22, 27, 46] have studied how overlapping will affect SPE. They consider different detectors, such as Advanced LIGO (AdvLIGO), LIGO Voyager, ground-based XG detectors (CE and ET), and space-based detector LISA [6] with different compact binary coalescences, including binary black holes (BBHs) [38, 27], binary neutron stars (BNSs) [34, 46], and neutron star–black hole (NSBH) systems [40]. The GW parameters used in these works are also different. In addition to the necessary parameters—binary masses, luminosity distance, and merger time—Himemoto *et al.* [22] considered the spin-orbit coupling and spin-spin coupling effects, and Hu *et al.* [23] considered the parameterized post-Newtonian coefficients to test general relativity and calculated the accumulating errors in the PE of OSs.

Qualitatively, when the merging times of different signals are close to each other, the mutual influence between the signals is expected to be more significant. In this case, the SPE results will have obvious biases, and we call the corresponding OS the

“biased OS”. In other words, the biased OSs are *real* OSs in the sense of PE. On the contrary, if the OS can be decomposed into individual signals and analyzed separately, we call it “unbiased OS”. Quantitatively, Relton *et al.* [38] and Himemoto *et al.* [22] stated that for an OS generated by two BBHs, it can be regarded as unbiased as long as the merger time difference Δt_c is larger than 0.1 s. The critical Δt_c given by Pizzati *et al.* [34] is more conservative, which is $\Delta t_c > 0.5$ s. Samajdar *et al.* [40] argued that in most cases, for the OS of two compact binaries the intrinsic parameters of each signal can be extracted with negligible biases. These inconsistencies are mainly caused by the different parameter choices. In addition, these works only pointed out whether the simulated OSs are biased OSs or unbiased OSs. They summarized the simulation results but did not systematically investigate the dependence of bias on the parameters.

In this work, we analyze the SPE biases of OSs generated by two BBHs, which is the basis to conduct PE for more complex OSs. Specifically, our work answers the following questions:

- (i) What is the origin of biases? In other words, why could there be biases when conducting SPE for OSs?
- (ii) How do the biases depend on the merger time of each component in the OS? Will large biases arise when the merger times are close?
- (iii) Given a target signal, what kind of signals are more likely to generate a biased OS when overlapping with it?

As mentioned above, it is difficult to directly describe the behaviors of bias in the whole parameter space. Therefore, we use the Fisher matrix (FM) method to quickly forecast the SPE biases for numerous OSs. The FM method can be regarded as an approximation of a full Bayesian analysis, and has been widely used to forecast and estimate parameters in GW researches [29, 16, 8, 26, 51, 43, 31, 50]. In particular, the FM method has also been applied in OS analysis [34, 22, 6].

As answers to the above questions, here we summarize our main conclusions:

- (i) Biases originate from the overlapping of the frequency evolution of signals. In the frequency domain, this is equivalent to a nearly constant phase difference between signals in a certain frequency band. For unbiased OSs, their component signals only overlap in the data stream in the time domain, but can be decomposed into independent signals and analyzed separately in the frequency domain.
- (ii) A small merger time difference is only a necessary condition for large biases. Although the bias is indeed larger when $\Delta t_c \sim 0$, there is a significant asymmetry in the order of the mergers. When the binary with lighter masses merges after the heavier one, the frequency evolution is easier to overlap, leading to a large bias. In addition, when $|\Delta t_c|$ increases, biases decay to zero in an oscillating way rather than monotonically. Moreover, the bias dependence on Δt_c is different for different parameters. The parameters can be divided into two categories according to whether they enter in amplitude or phase in the waveform. Varying Δt_c , when

the bias for one category is close to extreme values, the bias for the other category is almost zero.

- (iii) Biased OSs are more likely to arise when the component masses, especially the chirp masses, of individual signals are close. In this case, the frequency evolution of the two signals is so similar that large biases will occur in a wide range of Δt_c . In addition, the louder the other signal is, the larger the SPE bias of the target signal is.

It is worth noting that all the masses in the above conclusions are defined in the detector frame, since signals are overlapping in the detector data stream. When considering a detector network, the biases will depend on the relative locations between GW sources and detectors [38]. However, in each detector, the biases' behaviors are the same as we summarized above.

These conclusions are consistent with the intuitive understanding of the GW PE process, but they are analyzed and justified in detail for the first time in this work. In the attempt to obtain these conclusions, we establish an explicit expression [see Eq. (14)] and its corresponding analyzing pipeline for SPE bias. Benefiting from the rapidity of the FM method, this analyzing pipeline allows one to discuss and analyze the dependence of bias on various parameters easily.

In this paper, we also calculated the correlation coefficients between the corresponding parameters of two signals using the FM method. In this work, we detailedly calculate and compare the behaviors of correlation coefficients and biases. Their similar explicit expressions [see Eq. (14) and Eq. (22)] lead to their similar dependence on parameters. This is consistent with the qualitative results by Himemoto *et al.* [22]. Large correlation coefficients mean a strong indistinguishability and lead to a large bias in the SPE. Finally, to verify the validity of FM, we conduct a full Bayesian analysis for some representative OSs. For most OSs, the FM results are consistent with the full Bayesian SPE results. In the large-bias cases, there are slight differences between the FM method and the full Bayesian analysis. We justify the use of the FM method to forecast biases, which will provide a reference and guidance in the simulation of SPE and JPE for OSs.

The paper is organized as follows. Section 2 introduces the basic PE methods for GWs, including the full Bayesian inference and the FM approximation. In Section 3, we investigate the bias behaviors and analyze the origin of biases in depth using the FM method. Section 4 calculates the correlation coefficients of two signals and then compares them with the FM results. The applicability of the FM method in analyzing biases is verified using full Bayesian inference. Section 5 gives the summary and conclusion.

2. Parameter Estimation Methods

2.1. Basic concepts of Bayesian inference and FM approximation

The data $g(t)$ in a GW detector are the superposition of the GW strain $h(t; \boldsymbol{\theta})$ and the detector noise $n(t)$. In PE, we want to extract the GW parameters $\boldsymbol{\theta}$ from data $g(t)$. Using Bayes' theorem, one has the posterior distribution of $\boldsymbol{\theta}$,

$$P(\boldsymbol{\theta}|g) \propto p(\boldsymbol{\theta})P(g|\boldsymbol{\theta}), \quad (1)$$

where $p(\boldsymbol{\theta})$ is the prior, and $P(g|\boldsymbol{\theta})$ is called likelihood, which describes the conditional probability of collecting the data $g(t)$ given the parameters $\boldsymbol{\theta}$. Suppose that $n(t)$ is stationary and follows a Gaussian distribution with a mean of zero, the likelihood can be further expressed as [18]

$$P(g|\boldsymbol{\theta}) \propto e^{-\frac{1}{2}(g-h, g-h)}, \quad (2)$$

where the inner product (u, v) is defined for any two data streams, $u(t)$ and $v(t)$, as

$$(u, v) := 2\Re \int_{-\infty}^{\infty} \frac{u^*(f)v(f)}{S_n(|f|)} df = 4\Re \int_0^{\infty} \frac{u^*(f)v(f)}{S_n(f)} df, \quad (3)$$

where $S_n(f)$ is the one-sided power spectral density of the noise; $u(f)$ and $v(f)$ are the Fourier transforms of $u(t)$ and $v(t)$, respectively. Using $u(f)$ as example, the Fourier transform is defined by,

$$u(f) := \int_{-\infty}^{\infty} u(t)e^{-2\pi ift} dt. \quad (4)$$

In addition, we define the whitened data stream $u_w(f) := 2u(f)/\sqrt{S_n}$, which can be interpreted as the signal strength with respect to the noise in the frequency domain. Once the GW data $g(t)$ is obtained, one can construct the posterior distribution of the parameters $\boldsymbol{\theta}$ by the above formulas. After that, we can use some sampling techniques, such as the Markov-Chain Monte Carlo (MCMC) method [14, 15, 42] and Nested Sampling [44, 45], to obtain the posterior distributions of $\boldsymbol{\theta}$.

In principle, Bayesian inference gives the full posterior at the desired precision, but it can also take considerable computational time and resources, especially when the parameter space dimension is high. In contrast, the FM method is one of the fastest methods to give the approximate posterior, and it is widely used in the GW data analysis [48], where it reads

$$F_{\alpha\beta} = (h_{,\alpha}, h_{,\beta}), \quad (5)$$

where $h_{,\alpha} \equiv \partial h / \partial \theta^\alpha$ is the derivative of the waveform with respect to the α -th parameter, computed at the truth point $\tilde{\boldsymbol{\theta}}$ of the parameters. FM is a symmetric, positive semi-definite matrix, whose inverse exists in most cases in GW analysis [48, 49]. Denoting the inverse of FM as $\Sigma \equiv F^{-1}$, one obtain

$$\sigma_\alpha = \sqrt{\Sigma^{\alpha\alpha}}, \quad c_{\alpha\beta} = \frac{\Sigma^{\alpha\beta}}{\sigma_\alpha \sigma_\beta} = \frac{\Sigma^{\alpha\beta}}{\sqrt{\Sigma^{\alpha\alpha} \Sigma^{\beta\beta}}}. \quad (6)$$

Here, σ_α is the standard deviation of θ^α , $c_{\alpha\beta}$ is the correlation coefficient between θ^α and θ^β [29]. The FM approximation, which uses Eqs. (5) and (6) to obtain the errors and correlations of the parameters, is very fast to calculate, as it requires the derivative of the waveform only at one point. FM approximation is equivalent to the linearized-signal approximation [18, 48], that is, the dependence of the waveform template on the parameters is linear, which holds if and only if the GW signal is loud enough. In addition, when using the FM approximation result (6), we have defaulted that the priors of all parameters are uniform. In the frequentist view, the inverse matrix Σ is the covariance matrix of the maximum likelihood estimate (MLE) values $\hat{\theta}$ under linearized-signal approximation, and σ_α can be interpreted as (the lower limit of) measurement uncertainty due to the presence of noise [48].

2.2. PE methods of OSs

In the case of OSs, $h(t)$ should be the superposition of individual independent GW signals, then

$$g(t) = h(t; \tilde{\theta}) + n(t) = \sum_{j=1}^m h^{(j)}(t; \tilde{\theta}^{(j)}) + n(t), \quad (7)$$

where m is the number of GWs overlapping together, $h^{(j)}(t; \tilde{\theta}^{(j)})$ is the strain of the j -th signal, and $\tilde{\theta}^{(j)}$ is the corresponding true parameters. It should be noted that in practice the components of $g(t)$ are unknown; an OS can contain any number of GWs and the template corresponding to each signal can also be different [6].

When conducting PE, one can use different models to fit the GW strain. If the number of individual signals is known, and the parameters of all GWs are investigated simultaneously, one should take a model $h = h(t; \theta) = \sum_{j=1}^m h^{(j)}(t; \theta^{(j)})$, with $\theta = \{\theta^{(1)}, \dots, \theta^{(m)}\}$. This is called JPE [27]. In the SPE case, only one signal, $h^{(1)}$, and its corresponding parameters are considered. However, when conducting SPE, the strain data are still determined by Eq. (7). The presence of $\tilde{h}^{(2)}, \dots, \tilde{h}^{(m)}$ inevitably has an impact on the estimation of $\theta^{(1)}$, which leads to a bias in the SPE results.

For simplicity, we consider the likelihood function of SPE with the inclusion of two GW signals overlapping,

$$P(g(t)|\theta^{(1)}) \propto \exp \left\{ -\frac{1}{2} \left(\tilde{h}^{(1)} + \tilde{h}^{(2)} + n - h^{(1)}(\theta^{(1)}) \right), \right. \\ \left. \tilde{h}^{(1)} + \tilde{h}^{(2)} + n - h^{(1)}(\theta^{(1)}) \right\}. \quad (8)$$

With Eq. (8), one can exhaustively discuss how one signal in the OS affects the SPE of another signal. In principle, this requires exploring throughout the parameter space and comparing the SPE result with the truth $\tilde{\theta}^{(1)}$ and $\tilde{\theta}^{(2)}$. However, due to the limited computational resources, one in practice can only select some representative points for full Bayesian analysis, as was done in Refs. [40, 34, 38, 22]. It will be further discussed in Sec. 4.

Now, we use the FM method to derive the explicit expression of biases in SPE. Using linearized-signal approximation and expanding the waveform at the truth point, we have $h^{(1)}(\boldsymbol{\theta}^{(1)}) \approx \tilde{h}^{(1)} + \tilde{h}_{,\alpha}^{(1)}(\theta^{(1)\alpha} - \tilde{\theta}^{(1)\alpha})$, where $\tilde{h}_{,\alpha}^{(1)} \equiv \partial h^{(1)}(\boldsymbol{\theta}^{(1)})/\partial \theta^{(1)\alpha}$. Note that all quantities are computed at $\tilde{\boldsymbol{\theta}}^{(1)}$, and we have used the Einstein summation convention. Substituting it into Eq. (8) and using MLE, we obtain

$$\hat{\theta}^\alpha - \tilde{\theta}^\alpha = \Sigma^{\alpha\beta}(\tilde{h}_{,\beta}^{(1)}, n) + \Sigma^{\alpha\beta}(\tilde{h}_{,\beta}^{(1)}, \tilde{h}^{(2)}). \quad (9)$$

Since the SPE is only for $\boldsymbol{\theta}^{(1)}$, the superscript “(1)” of $\boldsymbol{\theta}$ is omitted for conciseness. To measure the deviation of the MLE results from the true value in the statistical sense, we use the most common approach, namely, the mean square error (MSE) [13], which is defined as the expected value of the square of the error $\hat{\theta}^\alpha - \tilde{\theta}^\alpha$

$$\text{MSE}_\alpha := \text{E} \left[(\hat{\theta}^\alpha - \tilde{\theta}^\alpha)^2 \right] = (\Delta\theta_{\text{bias}}^\alpha)^2 + \sigma_\alpha^2, \quad (10)$$

where $\text{E}[\cdot]$ means the ensemble average over the noise, $\Delta\theta_{\text{bias}}^\alpha := \text{E}[\hat{\theta}^\alpha] - \tilde{\theta}^\alpha = \Sigma^{\alpha\beta}(\tilde{h}_{,\beta}^{(1)}, \tilde{h}^{(2)})$ is called bias. Note this derivation has assumed stationary and Gaussian noise, and used the relation $\text{E}[(u, n)(n, v)] = (u, v)$ [18].

Equation (10) deserves a detailed discussion. Mathematically, the MSE can be decomposed into the sum of the square of the bias, and the variance of the estimator itself. The other signal, $\tilde{h}^{(2)}$, only contributes to the bias part in the MSE via $(\tilde{h}_{,\alpha}^{(1)}, \tilde{h}^{(2)})$, while the variance part has no relationship with $\tilde{h}^{(2)}$ and depends only on the sensitivity of the waveform to the parameters (via $\tilde{h}_{,\alpha}^{(1)}$) and the average strength of the noise S_n .

The MLE results are biased as long as $\Sigma^{\alpha\beta}(\tilde{h}_{,\beta}^{(1)}, \tilde{h}^{(2)}) \neq 0$, however, this is not the condition for biased OSs. In practice, if the bias $\Delta\theta_{\text{bias}}^\alpha$ caused by $\tilde{h}^{(2)}$ is much smaller than the statistical uncertainty $\Delta\theta_{\text{stat}}^\alpha$ caused by n , we can not conclude the bias in the results at all, but instead will attribute it to random errors caused by the noise or the sampling algorithm. Therefore, it is more meaningful to define the (dimensionless) reduced bias

$$B_\alpha := \frac{\Delta\theta_{\text{bias}}^\alpha}{\Delta\theta_{\text{stat}}^\alpha} = \frac{\Sigma^{\alpha\beta}(\tilde{h}_{,\beta}^{(1)}, \tilde{h}^{(2)})}{\sqrt{\Sigma^{\alpha\alpha}}}. \quad (11)$$

Note that in Eq. (11) only β is summed. Also, we omit the tilde sign since there is no essential difference whether the variable is $\boldsymbol{\theta}$ or $\tilde{\boldsymbol{\theta}}$. Once $h^{(1)}$ and $h^{(2)}$ are given, the reduced bias \mathbf{B} is determined by Eq. (11). Substituting \mathbf{B} into the expression of MSE, we obtain $\text{MSE}_\alpha = \sigma^2(B_\alpha^2 + 1)$. Now, it is easy to give a natural and simple criterion for biased OS: *for a certain OS, if there exists a component of \mathbf{B} larger than 1 or smaller than -1 , the OS is a biased OS; otherwise, the OS is an unbiased OS.*

3. Bias in the Overlapping of Two Individual Signals

3.1. Parameter selection and detector configuration

Now we use the method developed in Sec. 2 to study the behaviors of \mathbf{B} . Although the FM method quickly calculates the bias for given $\boldsymbol{\theta}^{(1)}$ and $\boldsymbol{\theta}^{(2)}$, exploring a high-dimensional parameter space is still not an easy task. As mentioned earlier, the focus

of this work is not to simulate several OS PEs as realistically as possible, but to discuss and explain the origin of SPE biases within a simple parameter space.

When generating the OSs, we get the nonspinning stellar-mass BBH signals using the IMRPHENOMD waveform template for $h^{(1)}$ and $h^{(2)}$ [25, 30]. The variable parameters are the chirp mass \mathcal{M} , the symmetry mass ratio η , the luminosity distance d_L , and the merger time t_c . In addition, we use the angle-averaged waveforms over the sky localization and inclination, as well as the polarization angle of GWs. This corresponds to a most conservative scenario, where two GW signals arrive at the detector from the same direction with the same inclination and polarization. Taking into account these angle parameters may reduce the biases [38], but this effect originates more from geometry than the intrinsic properties of PE. As for the merger phase ϕ_c , some studies pointed out that the merging phase difference can affect the appearance of biases significantly [34, 38], but no further analysis has been done. Here we take the merger phase between two signals $\Delta\phi_c = 0$ temporarily. After establishing the analysis process of biases, the $\Delta\phi_c \neq 0$ case can be easily incorporated into our analysis, and how it affects the biases can also be clearly explained. Finally, all parameters (especially the two mass parameters, \mathcal{M} and η) are defined in the detector frame, since the overlapping of GWs occurs in the detector rather than at the GW source location.

As for the detector, we choose the designed sensitivity of AdvLIGO‡ for the calculation of the inner product. The reason for this selection is essentially the same as Pizzati *et al.* [34]. On the one hand, although AdvLIGO is unlikely to detect OSs at present [35, 38], this is due to the low total event rate in the detection horizon of AdvLIGO. If two signals with close merging times are injected, a biased OS may occur. Also, the effective duration of a signal in AdvLIGO is much shorter than that in XG detectors, so the bias calculation is faster. On the other hand, the shape of the AdvLIGO sensitivity curve is similar to those of XG ground-based GW detectors (such as CE and ET), except that the sensitivity of AdvLIGO is about one order of magnitude lower. This means that the behaviors of an OS in AdvLIGO and XG detectors are similar, only differing roughly by a constant factor. Therefore, we expect the properties of biases with AdvLIGO sensitivity also apply to XG detectors. Moreover, as will be demonstrated in the following sections, the behaviors of bias in AdvLIGO is consistent with previous work, which considered OS in ET [22, 6]. This further increases the confidence in our conclusions based on OS simulations in AdvLIGO.

As a short summary, when generating an OS, we have eight free parameters, $\boldsymbol{\theta} = \{\mathcal{M}^{(1)}, \eta^{(1)}, d_L^{(1)}, t_c^{(1)}, \mathcal{M}^{(2)}, \eta^{(2)}, d_L^{(2)}, t_c^{(2)}\}$. The reduced bias $\mathbf{B} = \{B_{\mathcal{M}}, B_{\eta}, B_{d_L}, B_{t_c}\}$ is a 4-dimensional function defined on this 8-dimensional space. For convenience, we use indices $\alpha = \{1, 2, 3, 4\}$ for $\{\mathcal{M}, \eta, d_L, t_c\}$ respectively. In the following, we will analyze the properties of \mathbf{B} for each parameter.

‡ <https://dcc.ligo.org/LIGO-T1800044/public>.

3.2. Luminosity distance, signal-to-noise ratio and merger time

In the IMRPHENOMD waveform, the amplitude is inversely proportional to the luminosity distance d_L , while the phase is independent of d_L . This is relatively simple, so we analyze the dependence of \mathbf{B} on $d_L^{(1)}$ and $d_L^{(2)}$ first. For $d_L^{(2)}$, since $h^{(2)} \propto 1/d_L^{(2)}$, according to Eq. (11) we have $\mathbf{B} \propto 1/d_L^{(2)}$. As for $d_L^{(1)}$, since for $\beta \neq 3$,

$$h_{,\beta}^{(1)} \propto 1/d_L^{(1)}, \quad h_{,3}^{(1)} \propto 1/(d_L^{(1)})^2, \quad (12)$$

we have, for $\alpha, \beta \neq 3$,

$$\Sigma^{\alpha\beta} \propto (d_L^{(1)})^2, \quad \Sigma^{\alpha 3} \propto (d_L^{(1)})^3, \quad \Sigma^{33} \propto (d_L^{(1)})^4, \quad (13)$$

from the definition of FM and its inverse [Eqs. (5) and (6)]. Substituting them in Eq. (11), we find that $\mathbf{B} \propto (d_L^{(1)})^0 (d_L^{(2)})^{-1}$.

The luminosity distance directly affects the amplitude of GWs, which in turn affects the signal-to-noise ratio (SNR). For a GW signal h , its SNR is $\rho = \sqrt{\langle h, h \rangle}$. Since SNR is inversely proportional to d_L , we have $\mathbf{B} \propto (\rho^{(1)})^0 (\rho^{(2)})^1$. At first glance, this conclusion may seem strange, since the bias should be smaller for louder $h^{(1)}$. Note that the PE uncertainty is also smaller for louder signals, so the reduced bias \mathbf{B} does not depend on the strength of signal $h^{(1)}$. Similar results were mentioned by Antonelli *et al.* [6]. However, strictly speaking, this conclusion holds only when d_L varies or the sensitivity has been consistently increased or decreased by an overall factor. Signals with different internal parameters can have the same SNR, but lead to different biases.

Intuitively, for the merger time, \mathbf{B} should be related only to the merger time difference $\Delta t_c = t_c^{(2)} - t_c^{(1)}$ of the two signals. First, we decompose the frequency domain waveform into amplitude and phase, $h(f) = A(f)e^{i\phi(f)}$. It is easy to know that only $\phi(f)$ depends on t_c , and can be further written as $\phi(f) = \phi_0(f) - 2\pi f t_c$, where ϕ_0 is the phase when $t_c = 0$. On the other hand, Σ is only related to $\mathcal{M}^{(1)}$, $\eta^{(1)}$, and $d_L^{(1)}$, so \mathbf{B} depends on $t_c^{(1)}$ and $t_c^{(2)}$ only through the inner product $(h_{,\alpha}^{(1)}, h^{(2)})$, which is written explicitly as

$$\begin{aligned} (h_{,\alpha}^{(1)}, h^{(2)}) &= 4\Re \int_{f_{\min}}^{f_{\max}} \frac{A_{,\alpha}^{(1)} A^{(2)} - i\phi_{,\alpha}^{(1)} A^{(1)} A^{(2)}}{S_n(f)} e^{i(\phi_0^{(2)} - \phi_0^{(1)} - 2\pi f(t_c^{(2)} - t_c^{(1)}))} df \\ &= \int_{f_{\min}}^{f_{\max}} \mathcal{A}_\alpha^c \cos(\Delta\phi_0 - 2\pi\Delta t_c f) df + \int_{f_{\min}}^{f_{\max}} \mathcal{A}_\alpha^s \sin(\Delta\phi_0 - 2\pi\Delta t_c f) df, \end{aligned} \quad (14)$$

where $\mathcal{A}_\alpha^c \equiv 4A_{,\alpha}^{(1)} A^{(2)}/S_n$, $\mathcal{A}_\alpha^s \equiv 4\phi_{,\alpha}^{(1)} A^{(1)} A^{(2)}/S_n$, and $\Delta\phi_0 \equiv \phi_0^{(2)} - \phi_0^{(1)}$. The integration interval $[f_{\min}, f_{\max}]$ is determined by the sensitivity curve of AdvLIGO, independent of the OS parameters.

Mathematically, Eq. (14) is a modulated function integral, \mathcal{A}_α^c and \mathcal{A}_α^s are the modulation amplitudes, and the modulation phase $\Delta\phi_0$ is the phase difference between the two signals at $t_c^{(1)} = t_c^{(2)} = 0$ in the frequency domain. For the IMRPHENOMD

template, d_L appears only in the amplitude, so we have $\mathcal{A}_3^c \neq 0$ and $\mathcal{A}_3^s = 0$; t_c appears only in the phase, so $\mathcal{A}_4^c = 0$ and $\mathcal{A}_4^s \neq 0$. The intrinsic parameters \mathcal{M} and η contribute to both amplitude and phase, but numerical calculations show that $\mathcal{A}_{1/2}^s$ is about two orders of magnitude larger than $\mathcal{A}_{1/2}^c$, namely $\mathcal{A}_{1/2}^s \gg \mathcal{A}_{1/2}^c > 0$ (see [Appendix A](#)). This is because that the current matched filtering technique is more sensitive to the phase evolution of GWs. The phase ϕ_0 is only related to the internal parameters \mathcal{M} and η , and is generally a nonlinear function of f . As for $t_c^{(1)}$ and $t_c^{(2)}$, they only contribute to the arguments of trigonometric functions in the form of merger time difference Δt_c , which agrees with our expectation. Moreover, the contribution to the phase is a linear term of f .

According to the above discussion, we only need to explore a 5-dimensional parameter space, and the corresponding parameters are $\{\mathcal{M}^{(1)}, \eta^{(1)}, \mathcal{M}^{(2)}, \eta^{(2)}, t_c^{(2)} - t_c^{(1)}\}$. Therefore, unless specified, afterwards we fix $d_L^{(1)} = 500$ Mpc, $d_L^{(2)} = 3000$ Mpc, and $t_c^{(1)} = 0$.

3.3. Global dependence of biases on intrinsic parameters

The dependence of \mathbf{B} on d_L is only a simple rescale factor and does not touch on the real origin of biased OSs. To further shrink the parameter space, this subsection will take several sets of $\{\mathcal{M}^{(1)}, \eta^{(1)}, \mathcal{M}^{(2)}, \eta^{(2)}\}$ and study the generality of the dependence of \mathbf{B} on the internal parameters.

For $\{\mathcal{M}^{(1)}, \eta^{(1)}\}$, we will take 5 sets of parameters, expressed in terms of binary masses, with the Solar mass M_\odot as unit. The first set of parameters is intentionally taken as integers $(m_1^{(1)}, m_2^{(1)}) = (30, 20)$. We call this configuration the ‘‘TEST EVENT.’’ For the other 4 sets of parameters, we select the real GW events GW150914, GW190602_175927, GW190814, and GW190924_021846. GW150914 is the first GW event. GW190602_175927, GW190814, and GW190924_021846 are the events with the second largest chirp mass, the smallest mass ratio, and the lightest chirp mass, respectively, in GWTC-1 and GWTC-2. Finally, for each set of the above parameters, we calculate \mathbf{B} for $\Delta t_c \in [t_{\min}, t_{\max}] = [-0.1, 0.1]$ s. Most of the biased OSs occur in this range of Δt_c [[34](#), [38](#), [22](#)], which is also verified by the calculations below.

This subsection focuses on the dependence of \mathbf{B} on internal parameters, which means we need to choose some characteristic quantities to reflect the distribution \mathbf{B} in the range $\Delta t_c \in [-0.1, 0.1]$ s. In [Fig. 1](#), we show the dependence of \mathbf{B} ’s ‘‘max-max’’ and ‘‘max-mean’’ values on $m_1^{(2)}$ and $m_2^{(2)}$ when $(m_1^{(1)}, m_2^{(1)}) = (30, 20)$. To obtain the max-max (max-mean) values, we first calculate the maximum (mean) of $|B_\alpha|$ over $[t_{\min}, t_{\max}]$, then find the maximum value in the 4 (dimensionless) components of \mathbf{B} . We take the absolute value of B_α to identify biased OSs. In addition, to eliminate the effects of signal strength on biases, we adjust $d_L^{(2)}$ so that $\rho^{(2)} = 8$, which is the detection threshold of the ground-based detectors. The results of the other four sets of $m_1^{(1)}$ and $m_2^{(1)}$ are shown in [Appendix B](#).

We find that for a wide range of $m_1^{(2)}$ and $m_2^{(2)}$, the max-max value of \mathbf{B} is greater

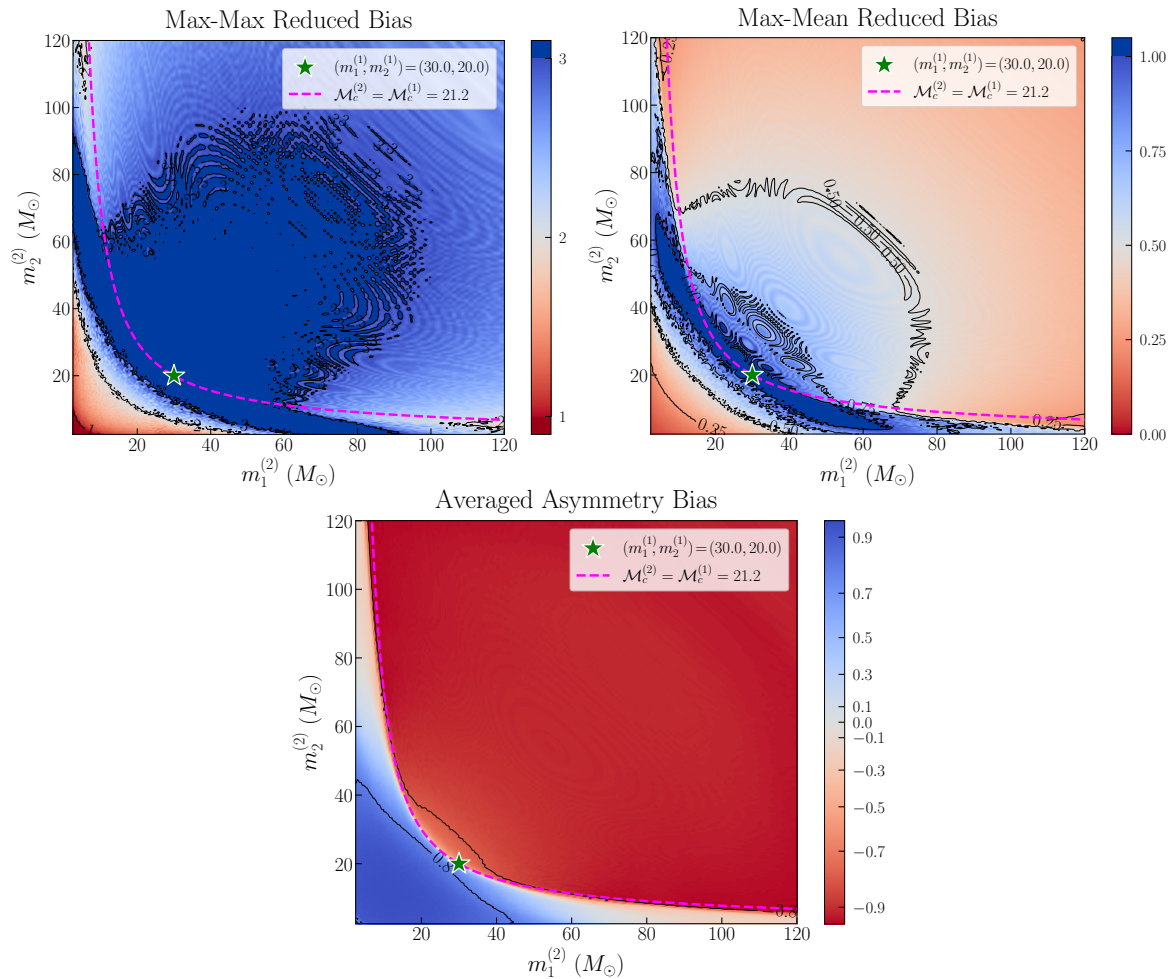


Figure 1: Dependence of the max-max value, max-mean value and average asymmetry of \mathbf{B} in the parameter space of $m_1^{(2)}$ and $m_2^{(2)}$ for the TEST EVENT. The location of $(m_1^{(1)}, m_2^{(1)})$ is marked with green stars. The magenta dashed lines indicate the values of $(m_1^{(2)}, m_2^{(2)})$ for which $\mathcal{M}^{(2)} = \mathcal{M}^{(1)}$.

than 1. This means that for almost any two GW signals, there exists a Δt_c making the corresponding OS biased. For the max-mean value, it is greater than 1 only in the region around $\mathcal{M}^{(2)} = \mathcal{M}^{(1)}$. Therefore, in the average sense, there is a higher probability of biased OS only when the chirp masses of the two signals are close. It should be noted that since \mathbf{B} is larger at $|\Delta t_c| \sim 0$ and decays to zero as $|\Delta t_c|$ increases, if the length of the Δt_c interval is shortened, e.g., to $|\Delta t_c| \in [-0.05, 0.05]$ s, the max-mean value will increase. However, the global behaviors of \mathbf{B} remain unchanged. Also, the max-max and max-mean values involve the absolute size of the bias, and we fix the SNR $\rho^{(2)} = 8$.

In addition to the absolute magnitude of the biases, we are also interested in their distribution with respect to Δt_c . One of the most important questions is whether there is a significant difference in the biases when $\Delta t_c > 0$ and $\Delta t_c < 0$, i.e., the dependence on the merger order. First, we define Asy_α as the difference between the area enclosed

by the horizontal axis $|B_\alpha|$ on $[-0.1, 0]$ s and the area on $[0, 0.1]$ s,

$$\text{Asy}_\alpha := \frac{\int_0^{t_{\max}} |B_\alpha| d\Delta t_c - \int_{t_{\min}}^0 |B_\alpha| d\Delta t_c}{\int_0^{t_{\max}} |B_\alpha| d\Delta t_c + \int_{t_{\min}}^0 |B_\alpha| d\Delta t_c}.$$

Then, we average Asy_α over the parameters of $\boldsymbol{\theta}^{(1)}$ to obtain the average asymmetry $\overline{\text{Asy}}$. $\overline{\text{Asy}}$ is a function of internal parameters $\{\mathcal{M}^{(1)}, \eta^{(1)}, \mathcal{M}^{(2)}, \eta^{(2)}\}$. When $\overline{\text{Asy}} > 0$, it means that the OS is more likely to be biased when $h^{(2)}$ merges after $h^{(1)}$. In addition, the closer $|\overline{\text{Asy}}|$ is to 1, the stronger the dependence of the bias on the merger order. For example, $\overline{\text{Asy}} = 0.8 = (9 - 1)/(9 + 1)$ means that the average bias on cases where $h^{(1)}$ merges first is 9 times of that where $h^{(2)}$ merges first. We calculate the average asymmetries of the above five sets of GW events and put the results of the TEST EVENT and the other four real GW events in Fig. 1 and Appendix B respectively. There is a clear boundary between $\overline{\text{Asy}} > 0$ and $\overline{\text{Asy}} < 0$. The boundary coincides with the $\mathcal{M}^{(2)} = \mathcal{M}^{(1)}$ curve. Roughly speaking, it is easier to generate a biased OS when the signal with heavier masses merges first. In addition, we found that the regions of small $|\overline{\text{Asy}}|$ (the white regions in the average asymmetry plot) are consistent with the regions of large bias (the dark blue regions in the max-max, max-mean plots).

Table 1: Parameter configurations of the six cases of $h^{(2)}$, where $M = m_1 + m_2$ is the total mass of binary. For $h^{(1)}$, we have $m_1 = 30.00 M_\odot$, $m_2 = 20.00 M_\odot$ and $d_L = 500$ Mpc.

Name	$m_1 (M_\odot)$	$m_2 (M_\odot)$	$M (M_\odot)$	$\mathcal{M} (M_\odot)$	η	d_L (Mpc)	ρ
EQUAL	30.00	20.00	50.00	21.24	0.240	3000	5.5
ASYMMETRIC	27.00	18.00	45.00	19.11	0.240	3000	5.1
ASYMMETRIC2	33.00	22.00	55.00	23.36	0.240	3000	5.9
RANDOM	40.00	34.00	74.00	32.08	0.248	3000	7.7
SYMMETRIC AND CLOSE	33.00	18.20	51.20	21.15	0.229	3000	5.4
SYMMETRIC AND NOT CLOSE	60.00	9.11	69.11	18.82	0.114	3000	3.8

3.4. Origin of biases

In Sec. 3.3, we vary $\{m_1^{(1)}, m_2^{(1)}, m_1^{(2)}, m_2^{(2)}\}$ and summarize the generality of the behaviors of \mathbf{B} with different internal parameters. Now we present the mathematical characteristics and physical interpretation of $B_\alpha(\Delta t_c)$ and draw the most important conclusion in our work: *the SPE biases originate from the overlapping of frequency evolution processes of the two signals*. To obtain this, we fix the internal parameters and investigate the relationship between \mathbf{B} and Δt_c . For $h^{(1)}$, we take $\boldsymbol{\theta}^{(1)}$ as the parameter in the TEST EVENT. For $h^{(2)}$, we take six representative sets of parameters,

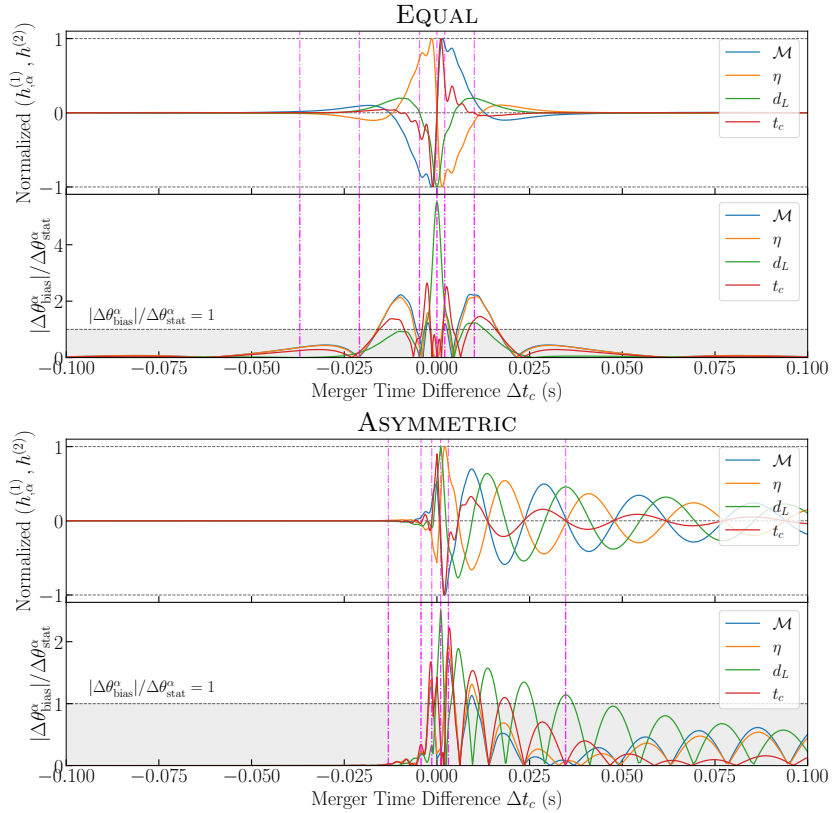


Figure 2: The dependence of $(h_{,\alpha}^{(1)}, h^{(2)})$ and $|B_\alpha| = |\Delta\theta_{\text{bias}}^\alpha|/\Delta\theta_{\text{stat}}^\alpha$ on Δt_c for EQUAL and ASYMMETRIC configurations. In the shaded area, $|B_\alpha| < 1$, which corresponds to unbiased OSs; the other region corresponds to biased OSs. The magenta dashed lines mark some representative Δt_c for reference.

called EQUAL, ASYMMETRIC, ASYMMETRIC2, RANDOM, SYMMETRIC AND CLOSE, SYMMETRIC AND NOT CLOSE, according to the relationship between $\boldsymbol{\theta}^{(2)}$ and $\boldsymbol{\theta}^{(1)}$ and the behavior of $\mathbf{B}(\Delta t_c)$. The parameters are listed in Table 1. In the main text, we only discuss the first two configurations to draw the main conclusion. The other four additional configurations provide a more comprehensive study in the parameter space, and we discuss them in the Appendix C.

According to Eqs. (11) and (14), the reduced bias B_α is just a linear combination of $(h_{,\alpha}^{(1)}, h^{(2)})$, and the combination coefficients only depend on $\boldsymbol{\theta}^{(1)}$. When $h^{(1)}$ is fixed, a large bias is roughly equivalent to a large $(h_{,\alpha}^{(1)}, h^{(2)})$, and the latter can be expressed as the sum of the integrals of two modulated trigonometric functions, which is easier to analyze. Thus, for each parameter configuration of $h^{(2)}$, we vary Δt_c within $[-0.1, 0.1]$ s, calculate $(h_{,\alpha}^{(1)}, h^{(2)})$ and the corresponding B_α , and display them in Fig. 2.

For the convenience of presentation, we define

$$D_\alpha(f) := \mathcal{A}_\alpha^c \cos(\Delta\phi_0 - 2\pi\Delta t_c f) + \mathcal{A}_\alpha^s \sin(\Delta\phi_0 - 2\pi\Delta t_c f),$$

$$R_\alpha(f) := \Sigma^{\alpha\beta} D_\alpha / \sqrt{\Sigma^{\alpha\alpha}},$$

which are the integrand functions of $(h_{,\alpha}^{(1)}, h^{(2)})$ and B_α , respectively. According to the dependence of \mathcal{A}^c and \mathcal{A}^s on the parameters, we have

$$D_1 \approx \mathcal{A}_1^s \sin \Delta\phi, \quad D_2 \approx \mathcal{A}_2^s \sin \Delta\phi, \quad (15)$$

$$D_3 \approx \mathcal{A}_3^c \cos \Delta\phi, \quad D_4 \approx \mathcal{A}_4^s \sin \Delta\phi, \quad (16)$$

where $\Delta\phi = \Delta\phi_0 - 2\pi\Delta t_c f$.

When $m_1^{(1)}$ and $m_2^{(1)}$ are fixed, the most special OS consists of two GWs with the same internal parameters, i.e., $(m_1^{(1)}, m_2^{(1)}) = (m_1^{(2)}, m_2^{(2)})$. We call this configuration EQUAL. In this case, $\Delta\phi_0 = 0$, and Eq. (14) degenerates to

$$(h_{,\alpha}^{(1)}, h^{(2)}) = \int_{f_{\min}}^{f_{\max}} \mathcal{A}_\alpha^c \cos(2\pi\Delta t_c f) df - \int_{f_{\min}}^{f_{\max}} \mathcal{A}_\alpha^s \sin(2\pi\Delta t_c f) df.$$

Thus, the modulation phase becomes a linear function of f , whose slope is proportional to Δt_c .

In Fig. 2, $(h_{,3}^{(1)}, h^{(2)})$ is an even function of Δt_c , while the other three components behave like odd functions. The d_L only contributes to the amplitude part of the waveform, then $\mathcal{A}_3^s = 0$. Therefore, $D_3(f; -\Delta t_c) = D_3(f; \Delta t_c)$ is an even function of Δt_c , and remains an even function after integration over f . Noting that t_c only contributes to the phase, we have $\mathcal{A}_4^c = 0$, so $(h_{,4}^{(1)}, h^{(2)})$ is an odd function. For \mathcal{M} and η , we have $\mathcal{A}^s \gg \mathcal{A}^c$. So D_α is dominated by \mathcal{A}^s , and both $(h_{,1}^{(1)}, h^{(2)})$ and $(h_{,2}^{(1)}, h^{(2)})$ are almost odd functions. As for $|B_\alpha|$, they are all basically even functions of Δt_c . The slight asymmetry originates from the linear combination of $(h_{,\alpha}^{(1)}, h^{(2)})$. Physically, the intrinsic parameters of the two signals are the same, and only the amplitudes are different. Therefore, the relationship between biases and merger time difference will inherit the symmetry.

Another thing is that the biases are large at $\Delta t_c \approx 0$, but small when $|\Delta t_c|$ is far away from 0. Obviously, the larger the difference in the merger times is, the smaller the bias will be. To explain this point quantitatively, we take some Δt_c and draw the corresponding $\Delta\phi(f)$, D_α , and R_α in Fig. 3. When $\Delta t_c = 0$, $|B_{d_L}| > 5$, while the other three parameters are almost unbiased. In this case, $D_\alpha = \mathcal{A}_\alpha^c$, and only \mathcal{A}_3^c significantly deviates from 0. In the EQUAL configuration and $\Delta t_c = 0$, the two signals only have the difference in amplitude, $h^{(1)} + h^{(2)} \propto h^{(1)}$. Therefore, the existence of $h^{(2)}$ is equivalent to slightly increasing the amplitude of $h^{(1)}$, leading to a large impact on the PE of d_L . The difference between $\Delta t_c = 2.1$ ms and $\Delta t_c = -37$ ms is only reflected in the slope of $\Delta\phi$ with respect to f . For the case of small Δt_c , $\Delta\phi$ changes slowly by π in the range of $0 \sim 200$ Hz. For all parameters, D_α is significantly nonzero, which eventually leads to large biases. However, in the $\Delta t_c = -37$ ms case, the rapid increase of $\Delta\phi$ leads to violent oscillations of D_α , which can not generate large biases after integration. This quantitatively explains why the biases are small for large Δt_c . At last, it is worth noting that $\Delta\phi$ always contains the $2\pi\Delta t_c f$ term that grows linearly with frequency, so this behavior can be applied to all mass configurations.

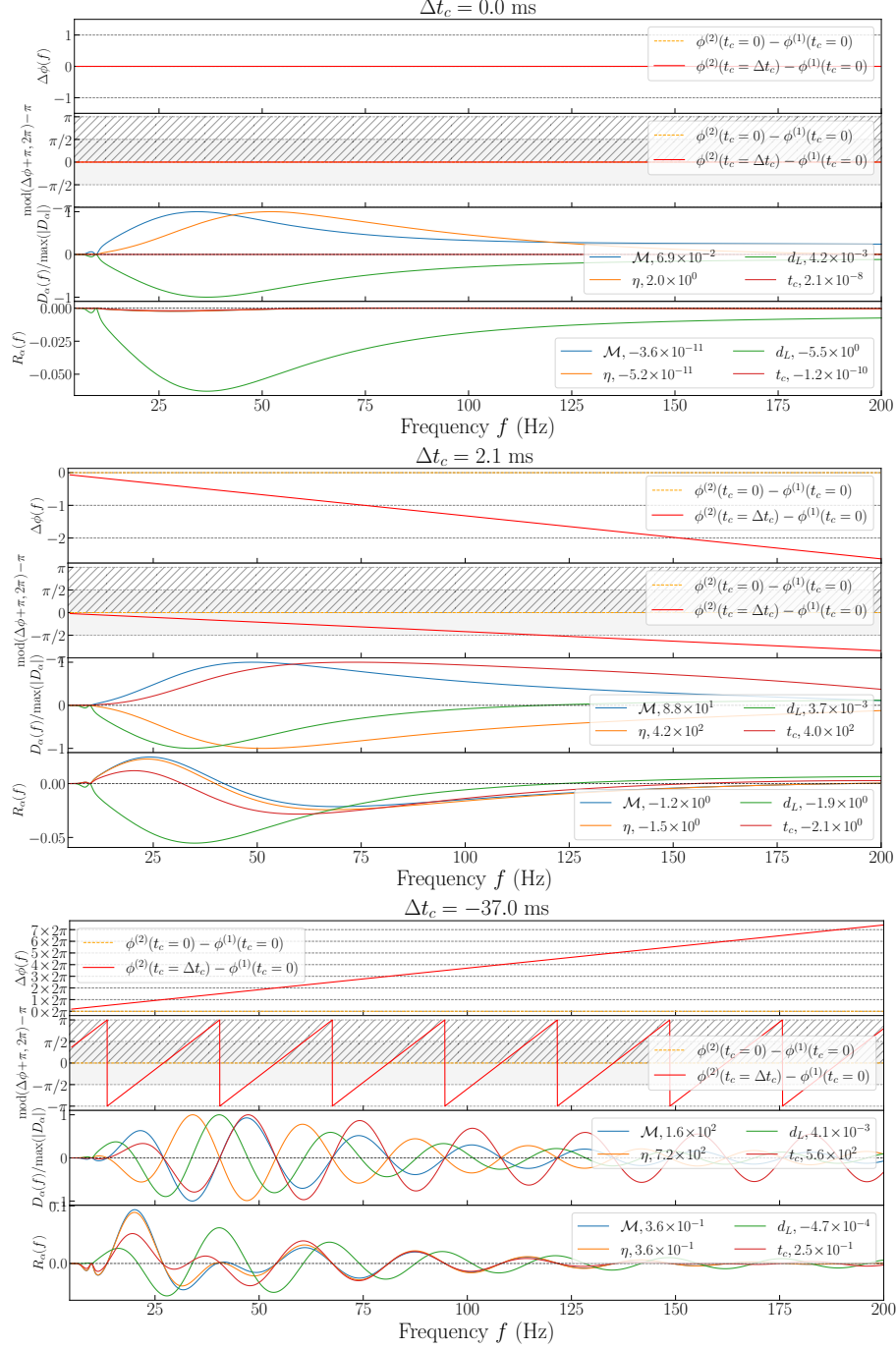


Figure 3: The dependence of $\Delta\phi(f)$, D_α , and R_α on the frequency f in the EQUAL configuration. The merger time differences are also marked. Note that the vertical variable ranges, such as $\Delta\phi$, in each subfigure are different. In the second row of each subfigure, the shaded area represents $-\pi/2 < \Delta\phi(f) < \pi/2$, while the hatched area means $0 < \Delta\phi(f) < \pi$. In the third row, the number after each parameter in the legend is the maximal value of $|D_\alpha|$. In the fourth row, the number means the integration of R_α over f , i.e. B_α .

In the EQUAL case, $\Delta\phi$ is completely determined by Δt_c , but for general mass configurations, we have to consider the contribution of a non-zero $\Delta\phi_0$. In the ASYMMETRIC (ASYMMETRIC2) configuration, we decrease (increase) $m_1^{(2)}$ and $m_2^{(2)}$ simultaneously, while keeping the mass ratio unchanged. Taking ASYMMETRIC as an example, we immediately find the asymmetry of \mathbf{B} on Δt_c , i.e., the significant dependence of the merging order. When $h^{(2)}$ merges after $h^{(1)}$, the biases are generally large. Otherwise, the biases can be ignored. Same as the EQUAL case, we also take some Δt_c as examples and show them in Fig. 4. Intuitively, we do expect the largest bias when two signals are “closest.” However, from the $B_\alpha(\Delta t_c)$ plot, we find that when $\Delta t_c = 0$ the bias is not maximum. In the following, we discuss how these larger biases arise, which correspond to those OSs with $\Delta t_c > 0$.

Mathematically, D_α is a modulated trigonometric function. The modulation amplitude is \mathcal{A}^c (\mathcal{A}^s), and the phase argument is $\Delta\phi = \Delta\phi_0 - 2\pi\Delta t_c f$. In order to generate a significant non-zero integral, one needs a large modulation amplitude and a stable $\Delta\phi(f)$. Since \mathcal{A}^c (\mathcal{A}^s) is large in the low-frequency band and slowly decays to 0 in the high-frequency band, combined with the behavior of $\Delta\phi_0$, we can divide the large bias cases into two categories according to the frequency band as follows.

- (i) Low-frequency band. In this case, $\Delta\phi_0$ changes drastically, but adding a larger linear term can make $\Delta\phi_0$ stable in a small range. Because \mathcal{A}^c (\mathcal{A}^s) is relatively large in the low-frequency band, a large bias can also be integrated in a short frequency range. In order to offset the drastic changes in $\Delta\phi_0$, the corresponding $|\Delta t_c|$ is large when biased in this way.
- (ii) High-frequency band. When f is high, $\Delta\phi_0$ changes approximately linearly, so it is easy to keep $\Delta\phi(f)$ to be a constant in a large frequency range by adding a linear term. Although \mathcal{A}^c (\mathcal{A}^s) is small at this time, a large bias can still be accumulated when integrating in a wide frequency band where $\Delta\phi(f)$ is stable. Since the change of $\Delta\phi_0$ in the high-frequency band is slow, the corresponding $|\Delta t_c|$ is also small.

In Fig. 4, we give examples of the two cases. When $\Delta t_c = 3.1$ ms, due to the existence of the linear term $-2\pi\Delta t_c f$, $\Delta\phi$ first increases and then decreases in the 50 ~ 150 Hz band. The change of monotonicity implies that $\Delta\phi$ basically stays around $\pi/2$ in the corresponding frequency band, leading to a large bias after integration. As for $\Delta t_c = 34.7$ ms, the monotonicity of $\Delta\phi$ changes in the 30 ~ 60 Hz band, producing a short stable stage for D_α and R_α . In this frequency band, both \mathcal{A}^c and \mathcal{A}^s also reach their maxima, so large biases can occur.

To sum up, as long as there is a relatively stable stage in the phase argument $\Delta\phi$, biased OSs are likely to arise. The location and even the presence of the stable stage are determined by Δt_c . With this in mind, we can explain why B_α oscillates and tends to 0 with the increase of $|\Delta t_c|$. Similar phenomenon has been noticed before, but not explored in detail [22]. Taking d_L as an example, the growth rate of $\Delta\phi_0$ about f gradually decreases, while the linear term $-2\pi\Delta t_c f$ contributes a constant negative growth rate.

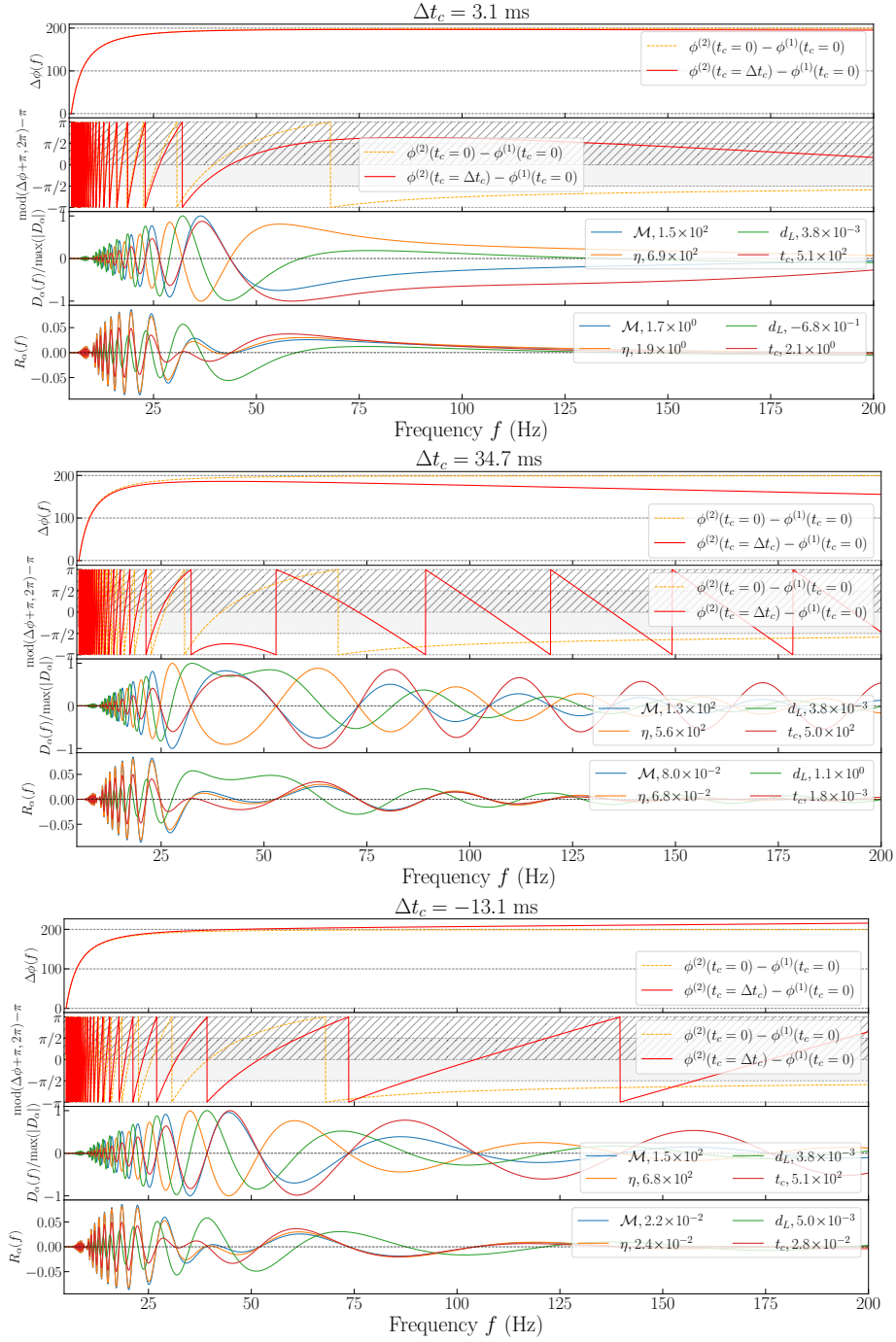


Figure 4: Same as Fig. 3, but for the ASYMMETRIC configuration.

Therefore, increasing Δt_c will cause the stable stage to shift left. On the other hand, since $\Delta\phi_0$ is changing between $-\pi$ and π (or equivalently, between 0 and 2π), the change of the horizontal position of the stable stage will be accompanied by the change of its vertical position. This means that, the stable value of $\Delta\phi$, which is denoted as ϕ_{sta} , will oscillate between $-\pi$ and π . For d_L , in the stable stage, $D_3 = \mathcal{A}_3^c \cos \Delta\phi \approx \mathcal{A}_3^c \cos \phi_{\text{sta}}$. If $\phi_{\text{sta}} \approx 0$ or π , we have $D_3 \approx 0$ and $(h_4^{(1)}, h_4^{(2)}) \approx 0$ after integration. As for B_3 , it is a linear combination of $(h_{,\alpha}^{(1)}, h_{,\alpha}^{(2)})$, and there still exists ϕ_{sta} making $B_3 \approx 0$. Therefore,

when Δt_c increases from 0, the stable stage moves to the left, and ϕ_{sta} oscillates between $-\pi$ and π , so B_3 also oscillates. When Δt_c further increases, the stable stage is very short, and the \mathcal{A}^c (\mathcal{A}^s) in this frequency band is small, then the cumulative bias is small in the stable stage. Outside the stable stage, $\Delta\phi$ changes rapidly with the frequency, and it is impossible to generate a large bias. Finally, we have $\mathbf{B} \rightarrow 0$.

As for the other three parameters, their corresponding D_α is dominated by $\mathcal{A}^s \sin \Delta\phi$. When $D_3 = 0$, the other D_α corresponding to $\alpha = 1, 2, 4$ will reach the extreme value. Therefore, when the bias of d_L is very small, the bias of the other three parameters is close to the maximum and vice versa. This is consistent with the results of numerical calculation, as shown in Fig. 2. Further, it is easy to explain why the biases are generally small when $\Delta t_c < 0$. Taking $\Delta t_c = -13.1$ ms as an example (see Fig. 4), both $-2\pi\Delta t_c f$ and $\Delta\phi_0$ are monotonically increasing with respect to f , and the phase argument changes more rapidly. So the oscillation of D_α is more violent than that when $\Delta t_c > 0$, and there is no stable stage and large bias. This explains the strong dependence of B_α on the merge order of the two signals.

Using the fact that biases are mainly generated at the stable stage, it is easy to analyze the dependence of biases on ϕ_c . The numerical results of Pizzati *et al.* [34] indicate that when $|\Delta t_c|$ is small the bias is very sensitive to the difference of merger phase $\Delta\phi_c = \phi_c^{(2)} - \phi_c^{(1)}$.[§] One can even turn a BOS into an UOS by adjusting $\Delta\phi_c$. Here we give an explanation. Adding the parameter $\Delta\phi_c \neq 0$, the phase argument becomes $\Delta\phi = \Delta\phi_0 + \Delta\phi_c - 2\pi\Delta t_c f$, and the stable value becomes $\phi_{\text{sta}} + \Delta\phi_c$. If $\phi_{\text{sta}} + \Delta\phi_c$ is close to 0 or π , then the D_α of \mathcal{M} , η , and t_c are also very close to 0. Even if there is a long stable stage, it is difficult to generate a large bias. On the contrary, the bias of d_L will be close to the extremum. Similar analysis can be applied to $\phi_{\text{sta}} + \Delta\phi_c \approx \pm\pi/2$, where the bias of d_L is small while biases of \mathcal{M} , η , and t_c reach their extrema.

Through the above analysis, we have understood the origin of biases mathematically. Physically, the biases come from the overlapping of the frequency evolution processes of the two signals, that is, in the same time period, the frequencies of the two signals are relatively close to each other. As an example, in the ASYMMETRY configuration, we find that it is easier to generate BOS when $h^{(2)}$ merges before $h^{(1)}$. The chirp frequency of the lighter binary is higher, so the frequency evolution processes are easier to “overlap” when it merges after the heavier one. Further, in Fig. 5, we show the whitened waveform, h_w , and the frequency evolution, $f(t)$, of two signals in the time domain for some representative Δt_c . For the case of $\Delta t_c = 3.1$ ms (34.7 ms), we note that the frequency band 50 ~ 150 Hz (30 ~ 60 Hz), where the chirp frequency of the two signals are relatively close, is also the frequency band where the phase difference in frequency domain $\Delta\phi$ is stable. The physical and mathematical explanations of the origin of biases are (and they must be) consistent. Generally speaking, the frequency of GW changes rapidly in the merger and ringdown stages, and only in the inspiral stage can there be a long overlapping period of the frequency evolution processes. On

[§] Note that the merger phase is originally defined in the time domain.

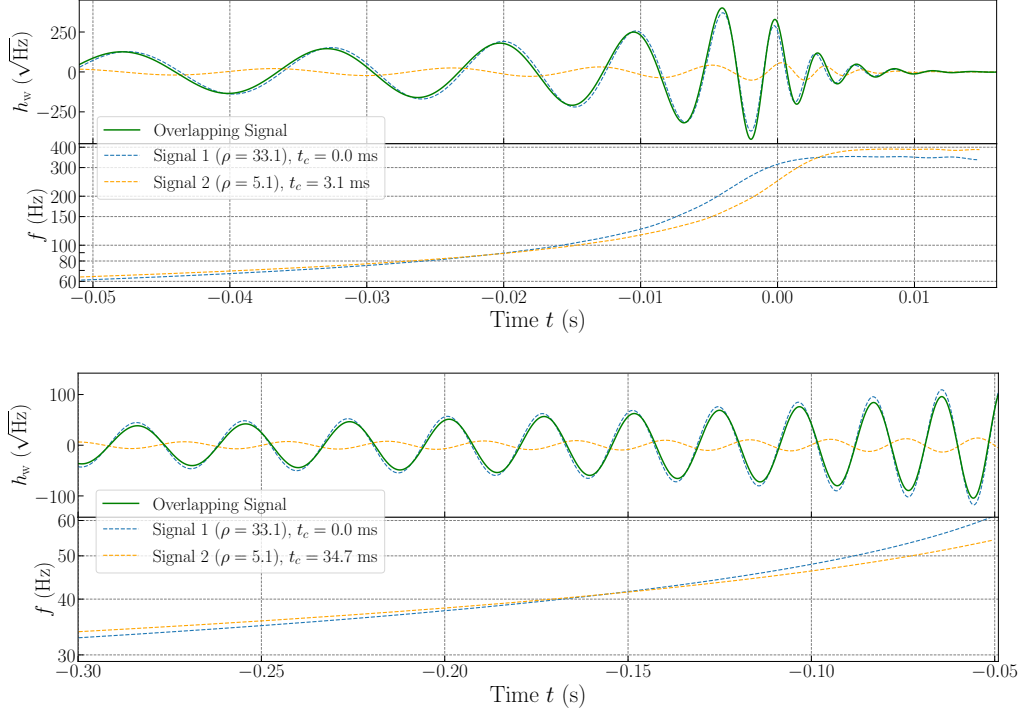


Figure 5: The whitened waveforms and frequency evolution diagrams of two signals in the time domain for the ASYMMETRIC configuration when Δt_c takes 3.1 ms and 34.7 ms.

the other hand, in the inspiral phase, the frequency domain phase and the frequency evolution have the relationship [12]

$$\frac{d\phi}{df} = -2\pi t(f). \quad (17)$$

Applying to $h^{(1)}$ and $h^{(2)}$, we have

$$\frac{d\Delta\phi}{df} \approx 0 \Leftrightarrow \frac{d\phi^{(1)}}{df} \approx \frac{d\phi^{(2)}}{df} \Leftrightarrow t^{(1)}(f) \approx t^{(2)}(f), \quad (18)$$

which shows that *the phase difference in the frequency domain keeps constant in a certain frequency band* and that *the frequency evolution processes overlap in the time domain* are equivalent. They just explain the origin of bias from different aspects. Both explanations are consistent with our intuitive understanding of the matched filtering technology. If the frequency evolution over time of the two signals is completely the same, it is impossible to separate the OS into individual ones. The strong degeneracy will influence the SPE, leading to large biases.

4. Other methods of analyzing biases

In this section, we verify the results and corresponding conclusions of biases in Sec. 3, using the correlation coefficients and the full Bayesian inference. We also point out the

feasibility of identifying biased OSs and unbiased OSs with FM in our analysis.

4.1. The correlation between two signals

In the previous section, we have used the SPE biases to characterize the effect of signal overlapping. When large biases occur, it indicates that the two signals have strong influences on the PEs of each other, i.e., the correlation between the two signals is large. Pizzati *et al.* [34] briefly studied the relationship between the correlation coefficient of the parameters of the two signals, as well as Δt_c under some specific configurations. However, they did not discuss the relationship between the correlation coefficients and the biases. Antonelli *et al.* [6] calculated some correlation coefficients and biases, but the result is limited to a rough qualitative analysis due to the high dimensionality of the parameter space. Here we calculate the correlation coefficients between the parameters of the two signals by the FM method, and focus on the relationship between the correlation coefficients and the biases. Here we only consider the correlation coefficients between the corresponding parameters of the two signals (for example, $\mathcal{M}^{(1)}$ and $\mathcal{M}^{(2)}$), which represent the main correlation between the two signals. The systematic analysis of the correlation coefficient between any two parameters (e.g., between $\mathcal{M}^{(1)}$ and $\eta^{(2)}$) is left to future work.

When calculating the correlation coefficients of the parameters between the two signals, the FM approximation should be applied to the JPE. The parameters are $\{\boldsymbol{\theta}^{(1)}, \boldsymbol{\theta}^{(2)}\}$, while the model takes $h(\boldsymbol{\theta}^{(1)}, \boldsymbol{\theta}^{(2)}) = h^{(1)}(\boldsymbol{\theta}^{(1)}) + h^{(2)}(\boldsymbol{\theta}^{(2)})$. According to Eq. (5), the FM is

$$F = \begin{bmatrix} F^{(1)} & M \\ M^\top & F^{(2)} \end{bmatrix}, \quad (19)$$

where $F^{(1)}$ and $F^{(2)}$ are the FM calculated when the parameters are taken as $\{\boldsymbol{\theta}^{(1)}\}$ and $\{\boldsymbol{\theta}^{(2)}\}$, respectively. The inverses of them are noted as $\Sigma^{(1)}$ and $\Sigma^{(2)}$. For the off-diagonal term, we have $M_{\alpha\beta} = (\partial_\alpha^{(1)} h^{(1)}, \partial_\beta^{(2)} h^{(2)}) = (h_{,\alpha}^{(1)}, h_{,\beta}^{(2)})$, and M^\top is the transposition of M . When $|\Delta t_c|$ is large, the correlation between the two signals is small, so each element of M will be much smaller than those of $F^{(1)}$ and $F^{(2)}$. In this case, the inverse of F can be written as

$$\Sigma = \begin{bmatrix} \Sigma^{(1)} & -\Sigma^{(1)} M \Sigma^{(2)} \\ -\Sigma^{(2)} M^\top \Sigma^{(1)} & \Sigma^{(2)} \end{bmatrix} + \mathcal{O}(M^2). \quad (20)$$

Ignoring the $\mathcal{O}(M^2)$ terms, the correlation coefficients between the corresponding parameters of the two signals are

$$c_{\theta^{(1)\alpha}\theta^{(2)\alpha}} = c_{\alpha,\alpha+4} = \frac{\Sigma^{(1)\alpha\beta} (\partial_\beta^{(1)} h^{(1)}, \partial_\gamma^{(2)} h^{(2)}) \Sigma^{(2)\gamma\alpha}}{\sqrt{\Sigma^{(1)\alpha\alpha} \Sigma^{(2)\alpha\alpha}}}. \quad (21)$$

Note that α is not summed in the above equation, and both $\{\boldsymbol{\theta}^{(1)}\}$ and $\{\boldsymbol{\theta}^{(2)}\}$ have 4 independent parameters. Correlation coefficients $c_{\alpha,\alpha+4}$ are linear combinations of the inner products $(h_{,\beta}^{(1)}, h_{,\gamma}^{(2)})$, and the combination coefficients are independent of Δt_c .

The expression of the correlation coefficients in Eq. (21) is very similar to the expression of the biases in Eq. (11), except for the element in the inner product. Therefore, we can use the analysis method in Sec. 3 to deal with them. According to Fig. 2, we find B_α and $(h_\alpha^{(1)}, h_\alpha^{(2)})$ have similar behaviors with respect to Δt_c , so are the positions of zeros and extrema. Mathematically, this means that using $\Sigma^{(1)\alpha\beta}$ to linearly combine $(h_\alpha^{(1)}, h_\alpha^{(2)})$ is similar to using a diagonal matrix. Applying this conclusion to Eq. (21), we only need to analyze the dependence of $(h_\beta^{(1)}, h_\gamma^{(2)})$ on Δt_c .

Like in Eq. (14), we explicitly write the expression of $(h_\beta^{(1)}, h_\gamma^{(2)})$

$$\begin{aligned} (h_\beta^{(1)}, h_\gamma^{(2)}) = & 4 \int_{f_{\min}}^{f_{\max}} \frac{A_{,\beta}^{(1)} A_{,\gamma}^{(2)} + A^{(1)} A^{(2)} \phi_{,\beta}^{(1)} \phi_{,\gamma}^{(2)}}{S_n} \cos(\Delta\phi_0 - 2\pi\Delta t_c f) df \\ & - 4 \int_{f_{\min}}^{f_{\max}} \frac{A_{,\beta}^{(1)} A^{(2)} \phi_{,\gamma}^{(2)} + A^{(1)} A_{,\gamma}^{(2)} \phi_{,\beta}^{(1)}}{S_n} \sin(\Delta\phi_0 - 2\pi\Delta t_c f) df, \end{aligned} \quad (22)$$

where $\Delta\phi_0$ is the same as in Eq. (14). Since the linear combinatorial effects of $\Sigma^{(1)}$ and $\Sigma^{(2)}$ are equivalent to diagonal matrices, we only need to consider the contribution of the diagonal elements. Take $\beta = \gamma = \alpha$, substitute them in Eq. (14) we have $c_{\alpha,\alpha+4} \propto (h_\alpha^{(1)}, h_\alpha^{(2)})$. For the luminosity distance, it does not contribute to the phase, i.e. $\phi_{,3} = 0$. For the merger time, $A_{,4} = 0$. As for \mathcal{M} and η , we have $A_{,\alpha} \ll A\phi_{,\alpha}$. Therefore, in the special case of $\beta = \gamma = \alpha$, the integral of $\sin \Delta\phi$ in Eq. (22) can always be insignificant, that is

$$(h_\beta^{(1)}, h_\gamma^{(2)}) \approx 4 \int_{f_{\min}}^{f_{\max}} \frac{A_{,\beta}^{(1)} A_{,\gamma}^{(2)} + A^{(1)} A^{(2)} \phi_{,\beta}^{(1)} \phi_{,\gamma}^{(2)}}{S_n} \cos(\Delta\phi_0 - 2\pi\Delta t_c f) df,$$

which is the modulation integral of $\cos \Delta\phi$. Therefore, we can expect the dependence of $c_{\alpha,\alpha+4}$ and B_3 (the bias of luminosity distance) on Δt_c to be almost the same.

In Fig. 6, we show the dependence of $(h_\alpha^{(1)}, h_\alpha^{(2)})$, correlation coefficients $c_{\alpha,\alpha+4}$, and B_α on the merger time difference Δt_c . For the sake of brevity, we only show the results of two configurations, ASYMMETRIC and SYMMETRIC AND NOT CLOSE, which can clearly reflect the oscillation of B_α . When $|c|$ is small ($\lesssim 0.5$), the behaviors of $c_{\alpha,\alpha+4}$ versus Δt_c are highly consistent with B_3 , and the positions of extrema and zeros are also similar. Correspondingly, for \mathcal{M} , η , and t_c , the zeros of their biases basically coincide with the extrema of $c_{\alpha,\alpha+4}$. When $|c|$ is large (such as the region around $\Delta t_c \sim 0$ in the ASYMMETRIC configuration), the oscillations of correlation coefficients and biases are more severe, but their basic trends are still similar, namely, c increases (decreases) when \mathbf{B} increases (decreases).

In this work, we only discuss the dependence of the relative size of correlation coefficients and biases on Δt_c . In fact, it is incorrect to expect that there can not be any biased OS when $|c|$ is small. For example, in the SYMMETRIC AND NOT CLOSE configuration, there is $|c| \lesssim 0.4$, but the maximum of B_α is about 1.5. For the ASYMMETRIC configuration, the maximum value of $|c|$ is close to 1, but the maximum of B_α is only slightly greater than 2. After rescaling the biases by the SNRs of the two

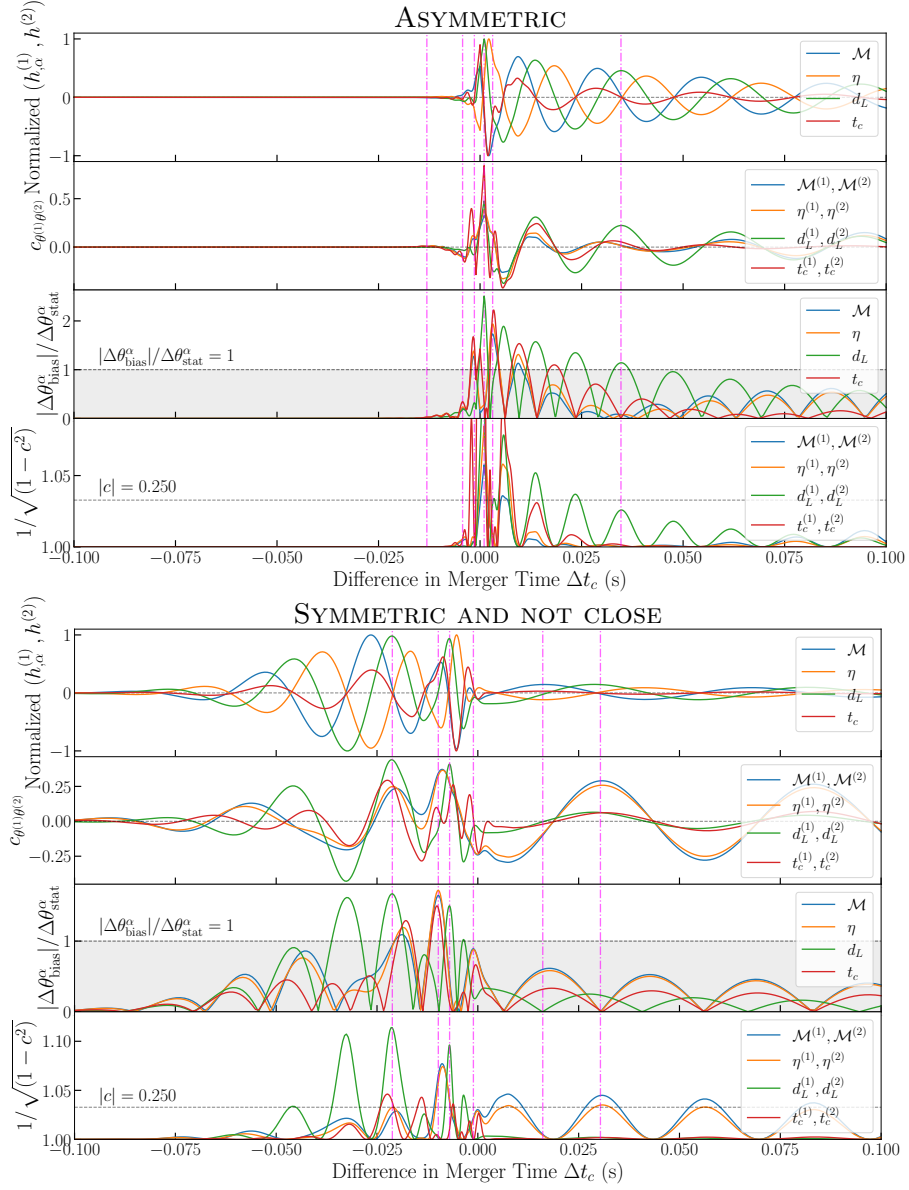


Figure 6: The dependence of biases and correlation coefficients on Δt_c in the SYMMETRIC AND NOT CLOSE configuration. The behaviors of $(h_{,\alpha}^{(1)}, h^{(2)})$ and $1/\sqrt{1-c^2}$ are also shown for comparison.

configurations, their maxima of biases have only small difference. On the other hand, when $|c|$ is large, the higher-order term of M in Eq. (20) cannot be ignored, and the relationship between correlation coefficients and biases will become more complicated.

The correlation between any two parameters can also be analyzed using Eq. (22). For example, if one wants to study the correlation between $d_L^{(1)}$ and $t_c^{(2)}$, taking $\beta = 3$ and $\gamma = 4$, only the $A_{,\beta}^{(1)} A_{,\gamma}^{(2)} \phi_{,\gamma}^{(2)}$ term is nonzero. Thus, Eq. (22) becomes the modulation integral of $\sin \Delta\phi$, so the correlation coefficient will behave similarly to B_4 . In addition, through simple calculation we have $c \propto (d_L^{(1)})^0 (d_L^{(2)})^0$. This means that the correlation coefficients do not depend on the strength of the two signals, which is consistent with our intuitive understanding.

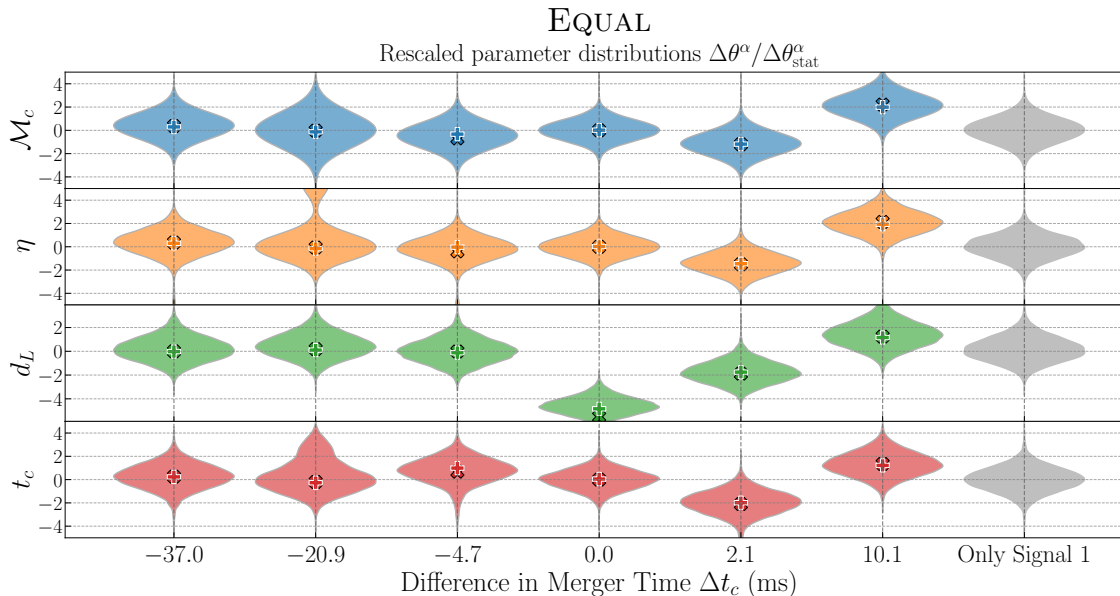


Figure 7: The SPE results in the EQUAL configuration, rescaled by the statistical uncertainty $\Delta\theta_{\text{stat}}$ from FM. The maximum likelihood points in the full Bayesian analysis and biases forecasted by the FM are labeled “+” and “x” respectively. For reference, the last column shows the SPE results when the data stream contains only the louder signal.

4.2. Full bayesian inference

So far, we have used the FM method to discuss the biases in SPE. This requires that the SNR of the target signal $h^{(1)}$ is large enough,^{||} and the biases are small enough to make linearized-signal approximation valid [18, 48]. Although the results obtained by FM in the previous sections are consistent with our physical intuition, in principle, it is always necessary to verify the applicability of the FM approximation. In this section, we select some representative points for the 6 group parameter configurations in Sec. 3.4, such as the extrema and zeros of B_α . We use Eq. (8) to perform full Bayesian PEs and compare them with the results in Sec. 3.

We use open source software package PARALLEL BILBY, ULTRANEST [7, 47, 39, 11] and the nested sampling Monte Carlo algorithm MLFRIENDS [9, 10] to conduct SPEs on $\theta = \{\mathcal{M}^{(1)}, \eta^{(1)}, d_L^{(1)}, t_c^{(1)}\}$. For \mathcal{M} , η , and t_c , we choose uniform priors. As for d_L , we first generate a uniform prior for the comoving volume V_c in the source frame, and then convert it in the parameter space of d_L . Different prior choices may affect PE results, but the difference between them can be ignored when $\rho^{(1)}$ is sufficiently large [48].

When injecting mock GW data, $g(t)$, different noise realizations also affect the PE results. Here we take $n = 0$, which is the most convenient case for generating data.

^{||} When calculating the correlation coefficients with the FM method, the SNRs of both $h^{(1)}$ and $h^{(2)}$ need to be large.

More importantly, as can be seen from Eq. (9), the deviation of the MLE result from the true value in this case is precisely the bias, $\Sigma^{\alpha\beta}(h_\beta^{(1)}, h^{(2)})$. It is not only reasonable, but also necessary to use the SPE results when $n = 0$ to verify the validity of FM [33].

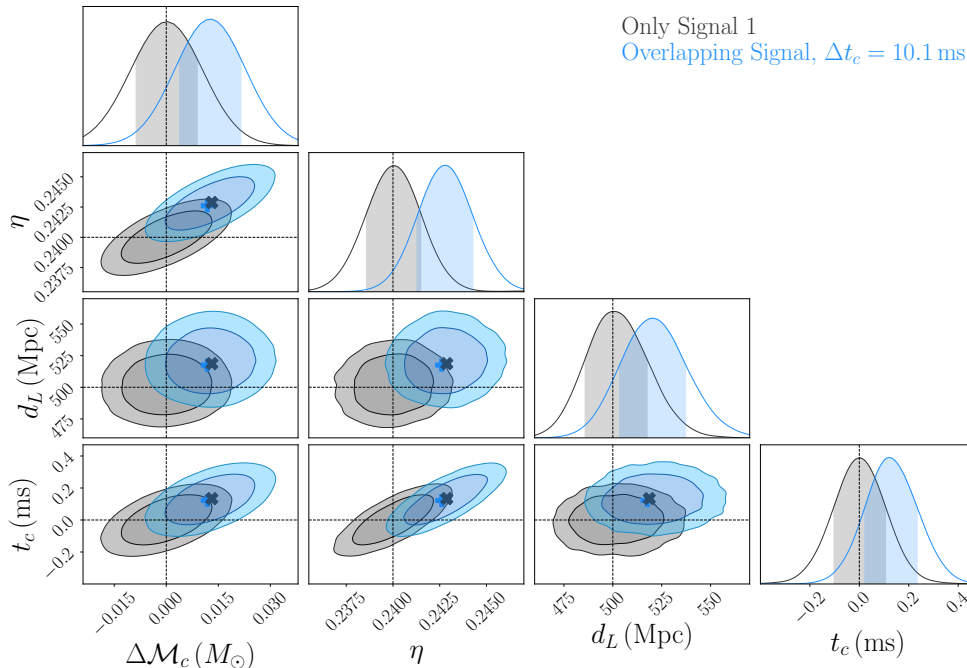


Figure 8: The contour plot of the parameters when $\Delta t_c = 10.1$ ms in the EQUAL configuration. The maximum likelihood points in the full Bayesian analysis and biases forecasted by the FM are labeled “+” and “x” respectively.

In Fig. 7, we show the marginalized distribution of each parameter in the EQUAL configuration, with Δt_c taken as those values corresponding to the magenta reference lines in Fig. 2. The biases calculated using FM in Sec. 3 are marked in the figure. The results of the other 5 groups of configurations are shown in Appendix D. For PE results with small biases, the difference between MLE and the truth is almost the same as the biases forecasted by the FM approximation. Furthermore, the contour plot of the parameters when $\Delta t_c = 10.1$ ms in the EQUAL configuration is shown in Fig. 8. In this case, all parameters have a large bias ($|B_\alpha| > 1$), but the forecasted biases of FM still highly coincide with the MLE of SPE.

5. Conclusion and Summary

With the continuous upgrading of GW detectors, more and more GW events will be detected. For next generation ground-based detectors, a large number of GW signals will overlap with each other [35, 40, 34, 38, 22]. In order to extract physical information from these OSs more efficiently and accurately, it is necessary to study the PE technology of OSs. However, before performing complex PE on the whole OS, it is important to understand how the PE of a specified signal in the OS is affected by other signals. This

effect is reflected in the bias between the SPE result and the true value of the specified signal. If the overlapping effects on each SPE are small, then the signals in the OS can be analyzed separately, and there is no need for the time-consuming JPE. So far, many works have discussed the SPE biases of OSs, covering various combinations of detectors, waveforms, and GW sources [35, 40, 34, 38, 22, 6, 27, 46, 23]. However, calculating lots of SPEs will cost considerable computing resources, and it is difficult to study the systematic dependence of bias on various parameters, resulting in our limited understanding of their behaviors.

In this work, we use the FM method to investigate the origin of biases in SPE and their dependence on GW parameters. Thanks to the fast computational speed of the FM method [18, 48, 49], we can explore the parameter space in more detail, and gain a deeper understanding of the biases. In Refs. [34, 6], the FM method was considered, but not treated as the primary tool to analyze biases. Here, with the help of FM, we establish an analytical expression of SPE biases in Sec. 2. We mainly studied the dependence of bias on the mass, luminosity distance, coalescence time, and phase, where OSs are generated by two BBH systems in AdvLIGO. Since the direct cause of OS is the overlapping of two signals in the time domain, the relationship between Δt_c and biases is particularly discussed in detail.

In Sec. 3, we find that there are large biases in the PE when the frequency evolutions of the two signals overlap to a large extent. In the frequency domain, this is equivalent to a constant phase difference between the two signals in the corresponding frequency band. This conclusion can also be intuitively obtained by considering the properties of matched filtering technology, but in this work, we give a rigorous and quantitative demonstration. For the whole parameter space, the existence of large biases is common, but biases are more likely to occur when the masses of the two signals, especially the chirp masses, are close. For most OSs, the biases strongly depend on the merger order of the two BBHs. When the binary with heavier component masses merges first, its frequency evolution is more likely to overlap with the other one, leading to large biases. The biases always reach their global extrema near $\Delta t_c \simeq 0$, and then oscillate and tend to zero with the increase of $|\Delta t_c|$. For a specific parameter, the behavior depends on how this parameter contributes to the waveform. The zero points of the bias of the parameter that mainly contributes to the frequency-domain phase are often the extreme points of the bias of the parameter that mainly contributes to the amplitude.

We also used other methods to analyze the bias behaviors. In Sec. 4, we calculate the correlation coefficient of the corresponding parameters of the two signals, and compare their behaviors with biases. Using the explicit expressions in Eqs. (14) and (22), we find that the behavior of correlation coefficients is similar to the bias of the parameter that mainly contributes to the amplitude. The numerical results verified this result (see Fig. 6). We also conducted full Bayesian inference on some representative parameter configurations to check the validity of the FM approximation. In conclusion, using FM to forecast the biases beforehand provides a powerful guidance for a full JPE or SPEs.

The main purpose of this work is to explain the origin of biases. For the

conciseness and universality of our conclusion, some secondary effects are ignored. In the future, the results of this work should be further extended before practical application. For parameters, we only selected the most critical ones including the binary masses, luminosity distance, merger time, and merger phase. When considering more parameters, such as the spins and the sky location, the PE error will likely increase, and the absolute size of the bias will also be affected. For detectors, we only considered OSs in AdvLIGO in this work and expect the bias behaviors to be similar to those in XG ground-based detectors, which is implied by recent works [6, 17, 22]. For long signals, one needs to consider the rotation of the Earth. For space-based detectors, the duration of each signal will be even longer, and biases in these detectors may have some special properties. Besides, the utilization of detector networks can also have a great impact on biases, depending on the merger times of two signals in different detectors [38]. For waveforms, the influence of waveform selection on bias can be studied. In addition, PE biases can come from other effects, such as inaccurate waveform modeling [23] and existence of glitches [19]. For the correlation between two signals, we pointed out the similarity between correlation coefficients and biases more quantitatively, extending the studies by Pizzati *et al.* [34] and Antonelli *et al.* [6]. Whether there is a numerical relationship between them remains to be discussed. Finally, the conclusions of this work can be probably extended to cases where more GW signals overlap. In the FM approximation, the bias caused by different GW signals can be linearly superimposed, so one will need to consider the biases led by every other signal one by one.

It should be pointed out that, this work focuses on understanding the PE behaviors from OSs, rather than seeking specific algorithms for analyzing OSs. In real GW detection, we do not know the true values of each signal, and even not know how many individual signals are present in the OS. The simple FM method can provide some insights for PE, but cannot replace a focused analysis. On the contrary, we expect that, the understanding of the mechanism of biases in OS will help develop a faster and more efficient PE algorithm, and serve in analyzing real OS events.

Acknowledgements

This work was supported by the National Natural Science Foundation of China (11975027, 12147177, 11991053, 11721303), the China Postdoctoral Science Foundation (2021TQ0018), the National SKA Program of China (2020SKA0120300), the Beijing Municipal Natural Science Foundation (1242018), the Max Planck Partner Group Program funded by the Max Planck Society, and the High-Performance Computing Platform of Peking University. J. Z. is supported by the “LiYun” Postdoctoral Fellowship of Beijing Normal University, and C. L. is supported by the China Scholarship Council (CSC).

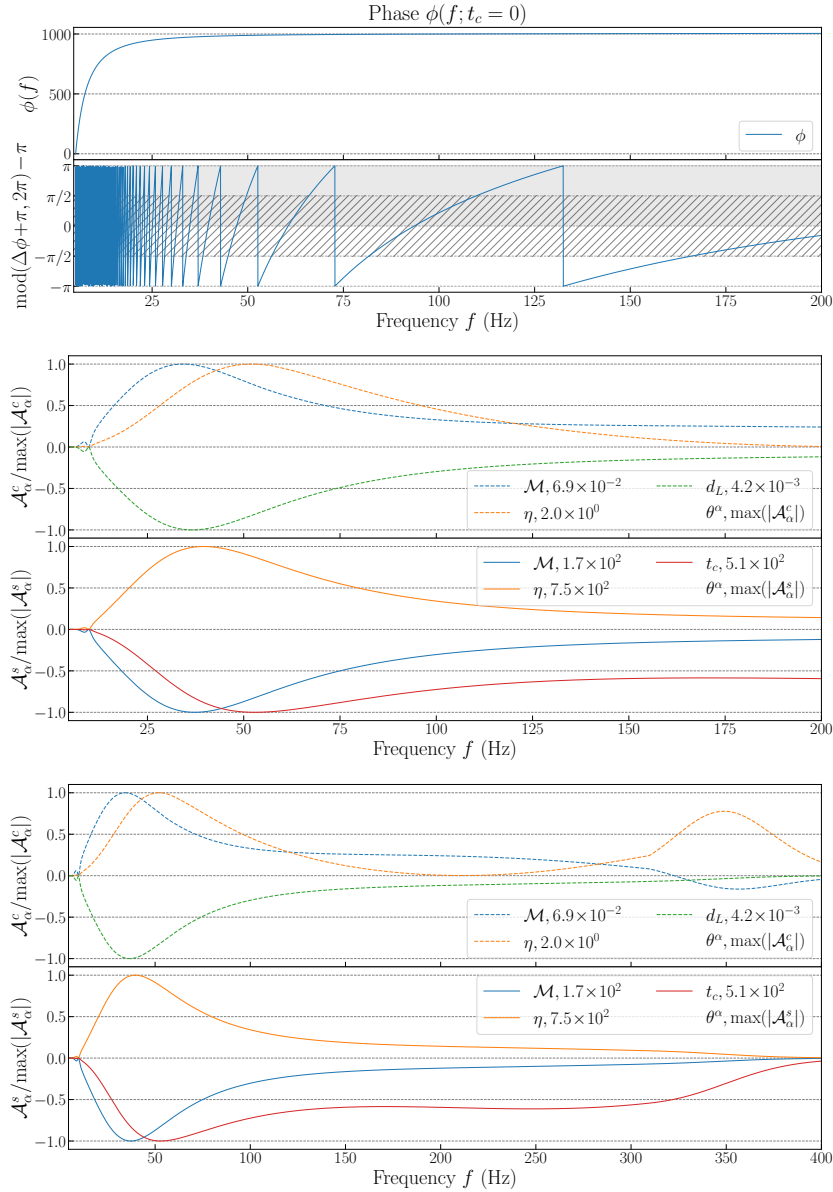


Figure A1: The frequency-domain phase, $\phi(f)$, and the normalized modulation amplitudes, \mathcal{A}_α^c and \mathcal{A}_α^s , of the waveform. The number after each parameter is the maximum value of the corresponding normalized modulation amplitude.

Appendix A. Waveforms and derivatives of waveforms

Figure A1 shows the frequency-domain phase of the IMRPHENOMD waveform template, as well as the derivatives of the waveform (expressed by \mathcal{A}_α^c and \mathcal{A}_α^s). Note that $\mathcal{A}_3^s = 0$ and $\mathcal{A}_4^c = 0$ are not drawn. The injected parameters are $\{m_1 = 30 M_\odot, m_2 = 20 M_\odot, d_L = 500 \text{ Mpc}, t_c = 0\}$. The frequency-domain phase grows rapidly in the low frequency band ($\lesssim 25 \text{ Hz}$), while in the high frequency band ($\gtrsim 100 \text{ Hz}$) it grows slowly and approximately linearly. The modulation amplitude typically reaches the maximum value within 30–50 Hz, consistent with the most sensitive frequency band of AdvLIGO.

Also, for \mathcal{M} and η , \mathcal{A}_α^s is at least two orders of magnitude larger than \mathcal{A}_α^c .

Appendix B. Max-max and max-mean of reduced biases

Figure B1 shows the dependence of the max-max value, max-mean average value, and average asymmetry of \mathbf{B} on $(m_1^{(2)}, m_2^{(2)})$. The mass components $(m_1^{(1)}, m_2^{(1)})$ are taken as the masses in the detector reference system of GW events GW150914, GW190602_175927, GW190814, and GW190924_021846. Their behaviors are similar to those in Fig. 1. When $\mathcal{M}^{(2)} \approx \mathcal{M}^{(1)}$, large biases occur, and the average asymmetry is close to 0.

Appendix C. SPE biases behaviours in other internal parameter configurations

In the main text, we demonstrate that the biases come from the overlapping of frequency evolution. After understanding the origin of biases, it is easy to understand the global dependence of biases on intrinsic parameters in Sec. 3.3 as follows.

- (i) For a given detector, its sensitive frequency band is fixed. Due to the selection effect of the detector, the characteristic frequencies of the detected signals are similar (~ 100 Hz for AdvLIGO). As long as the merger time difference is appropriate, it is easy to make the corresponding frequency evolutions overlap in the time domain. This explains why biased OSs are inevitable.
- (ii) For two GW signals with similar mass components, the frequency evolutions are also similar. Therefore, they can easily overlap for a wide range of Δt_c , and the stable stage of $\Delta\phi$ is longer, which is more likely to produce large biases on average.
- (iii) The frequency evolution $f(t)$ is strongly dependent on the masses of the GW source. As long as the masses of two GW signals are not particularly close, their evolution behaviors will be significantly different. Obviously, when the signal with a lower frequency merges first, it is easier to overlap with the frequency evolution of the signal with a higher frequency, which produces a strong dependence of the biases on the merger order. On the contrary, if the masses of the two signals are close, it does not matter which one merges first, so $|\overline{\text{Asy}}|$ is small. At the same time, according to (ii), the biases in these cases are large in the average sense. This explains the consistency between the regions where $|\overline{\text{Asy}}| \sim 0$ and those where the bias is large.

Without loss of generality, we selected three representative configurations in the $(m_1^{(2)}, m_2^{(2)})$ parameter space, namely ASYMMETRIC2, RANDOM, SYMMETRIC AND CLOSE, SYMMETRIC AND NOT CLOSE to further validate these conclusions.

For the ASYMMETRIC2 configuration, it is equivalent to exchanging the positions of $h^{(1)}$ and $h^{(2)}$, and $\Delta\phi$ is monotonically decreasing with respect to f . Therefore, biased OSs will mainly occur when $\Delta t_c < 0$, which is consistent with the results in Fig. C1. For

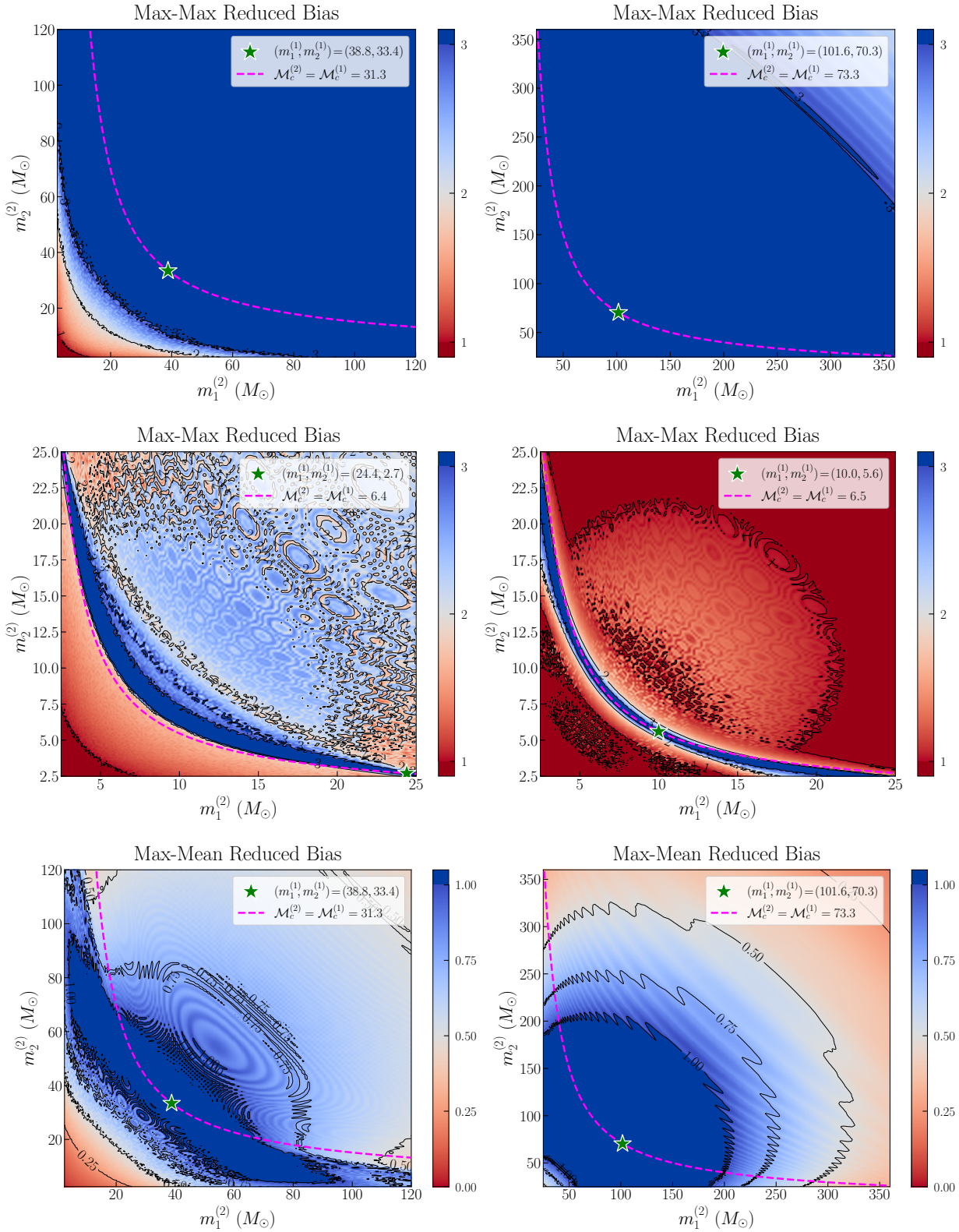


Figure B1: Same as Fig. 1, but the parameters are taken from real GW events.

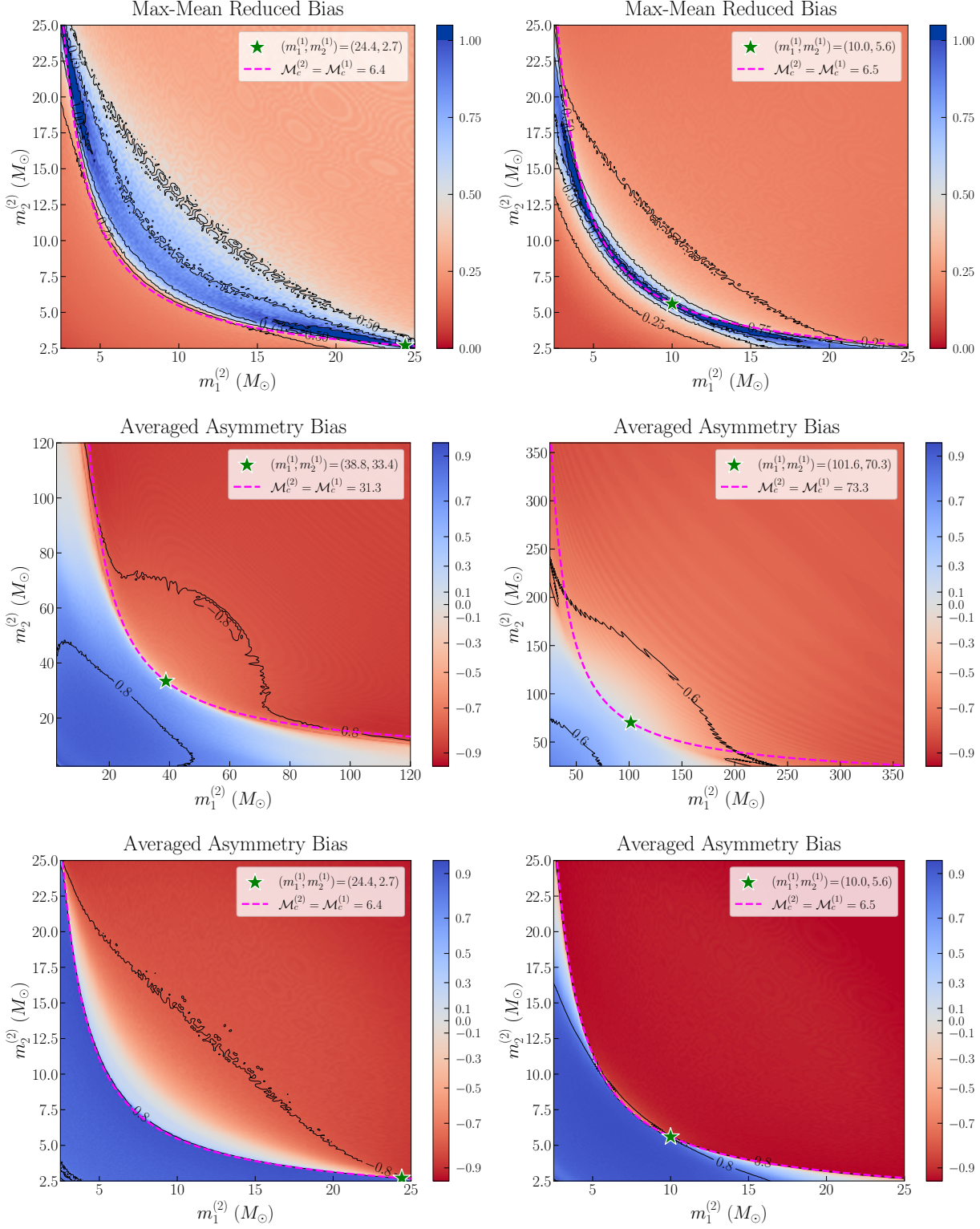


FIG. B1 (continued).

the RANDOM configuration, the source masses of $h^{(2)}$ are significantly larger than that of $h^{(1)}$, so we expect that large biases mainly occur when $\Delta t_c < 0$, and the dependence

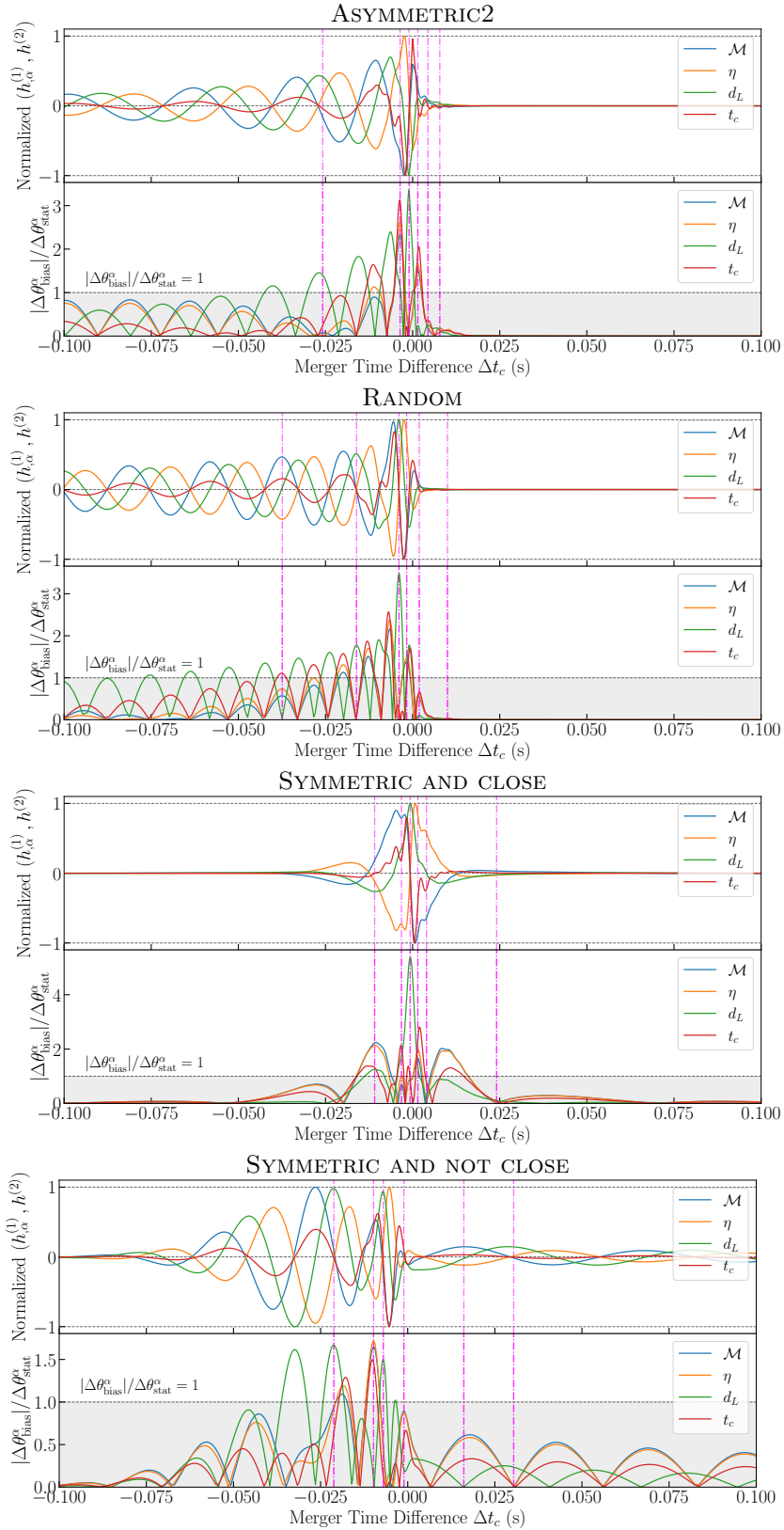


Figure C1: Same as Fig. 2, but for the ASYMMETRIC2, RANDOM, SYMMETRIC AND CLOSE, and SYMMETRIC AND NOT CLOSE configurations.

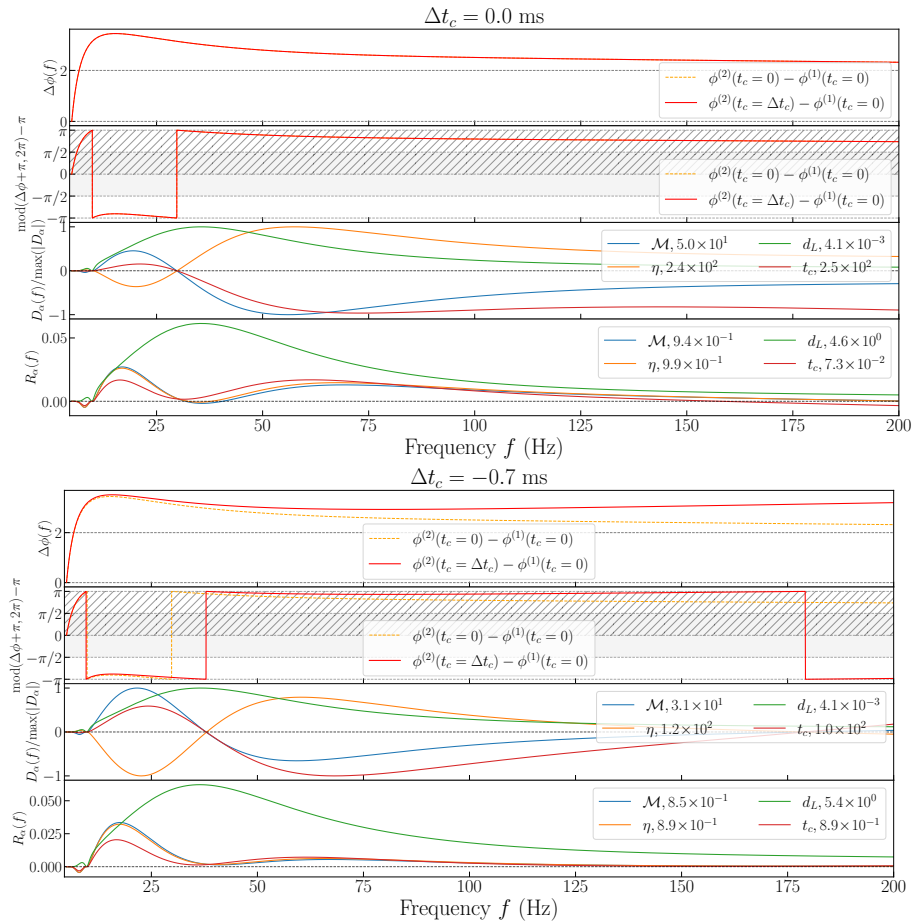


Figure C2: Same as Fig. 3, but for the SYMMETRIC AND CLOSE configuration.

of the bias on Δt_c should be similar to the ASYMMETRIC2 configuration. The results in Fig. 2 verified this. Further, for most $(m_1^{(2)}, m_2^{(2)})$ in the parameter space, their $|\overline{\text{Asy}}|$ is close to 1, showing a strong asymmetry of their bias behaviors. Therefore, ASYMMETRIC and ASYMMETRIC2 configurations can represent the dependence of biases on Δt_c for most OSs whose masses of two signals are not similar.

Next, we discuss the parameter configurations where $|\overline{\text{Asy}}| \sim 0$. For the SYMMETRIC AND CLOSE configuration, we choose $m_1^{(2)}$ to be slightly larger than $m_1^{(1)}$, and then adjust $m_2^{(2)}$ such that $|\overline{\text{Asy}}|$ is minimal. It can be seen that \mathbf{B} is approximately symmetrical about Δt_c . This is very similar to the EQUAL configuration, except that all $B_\alpha(t)$ curves are slightly moved to the left. Same as before, we take some Δt_c to calculate the frequency-domain phase, which is shown in Fig. C2. When $\Delta t_c = 0$, we find that the overall change of $\Delta\phi_0$ under this configuration is not large, and it increases with f first and then decreases. The change of monotonicity leads to a long stable stage, i.e., a large bias. This is significantly different from the ASYMMETRIC configuration, where $\Delta\phi_0$ increases monotonically with f , which requires additional non-zero Δt_c to generate a significantly stable stage.

In the SYMMETRIC AND CLOSE configuration, $\Delta\phi_0$ does not change much with

f , which is why \mathbf{B} behaves similarly to the EQUAL configuration. When Δt_c significantly deviates from 0, $|2\pi\Delta t_c f|$ will be much larger than $|\Delta\phi_0|$ for most f , so $\Delta\phi = \Delta\phi_0 - 2\pi\Delta t_c f \approx -2\pi\Delta t_c f$, which is exactly the phase difference in the EQUAL configuration. Of course, on the basis of the relatively stable $\Delta\phi_0$, we can slightly adjust Δt_c to make $\Delta\phi$ more stable. When $\Delta t_c = -0.7$ ms, $\Delta\phi$ is very close to $\pm\pi$ in a wide frequency band, making the bias larger. In other words, when $\Delta t_c = -0.7$ ms, the behavior of $\Delta\phi$ is more like a constant, so the symmetry axis of \mathbf{B} will move to $\Delta t_c = -0.7$ ms. This explains the slight movement of the bias curves in the SYMMETRIC AND CLOSE configuration.

Physically, the process of adjusting $m_2^{(2)}$ is equivalent to finding a $h^{(2)}$ whose frequency evolution is most similar to $h^{(1)}$. As long as the frequency evolution behavior of the two signals is similar, there will be a long overlapping of the frequency evolutions no matter which binary merges first, and the corresponding $|\overline{\text{Asy}}|$ is small. Therefore, if $m_1^{(2)} > m_1^{(1)}$, to minimize $|\overline{\text{Asy}}|$ one must have $m_2^{(2)} < m_2^{(1)}$. Otherwise, $h^{(2)}$ is generated by a heavier binary, leading to similar results to that of the ASYMMETRIC2 case.

Finally, we discuss the influence of η on the bias or the bias behaviors of binaries with extreme mass ratios. In general, the frequency evolutions are mainly determined by the chirp mass \mathcal{M} . This is why we take $\eta^{(2)} = \eta^{(1)}$ in the ASYMMETRIC and ASYMMETRIC2 configurations. In the SYMMETRIC AND NOT CLOSE configuration, we fix $m_1^{(2)} = 2m_1^{(1)}$ and adjust $m_2^{(2)}$ to minimize $|\overline{\text{Asy}}|$. Obviously, to obtain a similar frequency evolution, $m_2^{(2)}$ must be small. Interestingly, at this time, although $M^{(2)} > M^{(1)}$, there is $\mathcal{M}^{(2)} < \mathcal{M}^{(1)}$. This phenomenon was mentioned in Sec. 3.3, that is, when $(m_1^{(1)}, m_2^{(1)}) = (30, 20)$, the region where $|\overline{\text{Asy}}|$ is small locates below the line where $\mathcal{M}^{(2)} = \mathcal{M}^{(1)}$. In Fig. C3, we draw $\Delta\phi(f)$, D_α , R_α , whitened waveforms and frequency evolutions of the two signals when $\Delta t_c = -9.8$ ms. Although $\mathcal{M}^{(2)} < \mathcal{M}^{(1)}$, $m_1^{(2)}$ (also $M^{(2)}$) is too large. In general, the frequency of $h^{(2)}$ is still lower than $h^{(1)}$. In other words, the frequency of a GW signal with an extreme mass ratio is lower, so smaller chirp masses will be needed to generate a similar frequency evolution to $h^{(1)}$. Therefore, in Fig. 2, the region where $|\overline{\text{Asy}}| \sim 0$ locates below the line where $\mathcal{M}^{(2)} = \mathcal{M}^{(1)}$. On the contrary, if η is small, such as GW190814, the region will be above (see Fig. B1).

Back to the SYMMETRIC AND NOT CLOSE configuration, in fact, the biases are not asymmetric about Δt_c , but just distributes on $\Delta t_c < 0$ and $\Delta t_c > 0$ evenly. In this configuration, although $\Delta\phi_0$ also has a stable stage similar to that in the SYMMETRIC AND CLOSE configuration, the source masses and the frequency evolutions of the two signals, are too different. So one cannot expect \mathbf{B} to have an obvious symmetric axis about Δt_c . However, in this case, we can still choose an appropriate Δt_c to increase the length of the stable stage and cause a large bias. The use of $\Delta t_c = -9.8$ ms is an example, and its behavior will not be described repeatedly here.

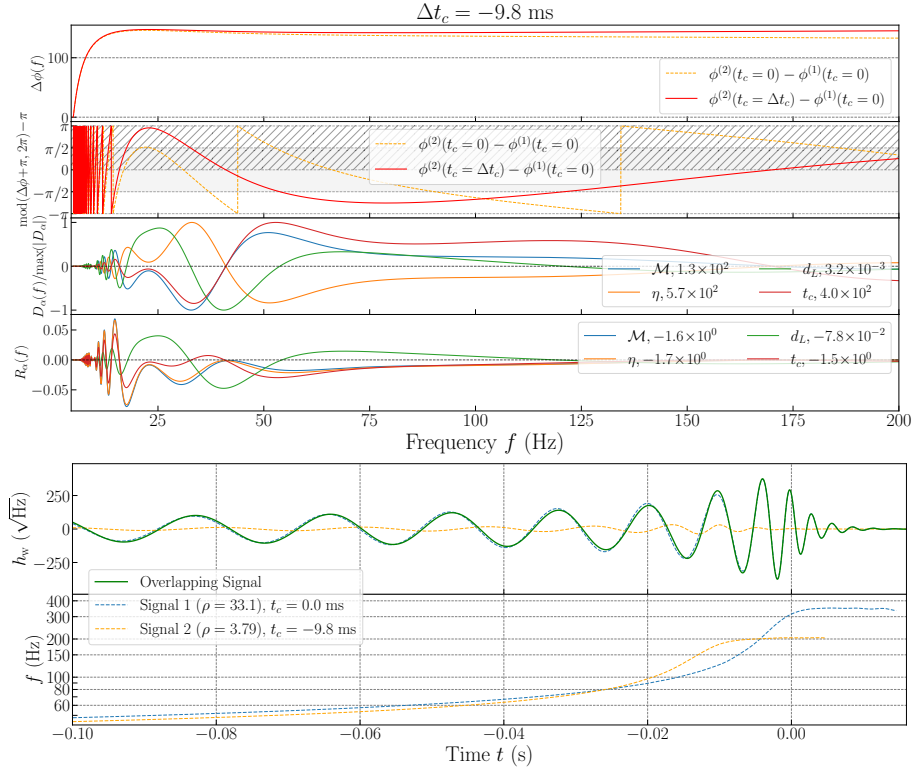


Figure C3: Same as Fig. 5, but for the SYMMETRIC AND NOT CLOSE configuration and $\Delta t_c = -9.8$ ms.

Appendix D. Full Bayesian SPE results in other internal parameter configurations

Figure D1 shows the marginalized distribution of parameters in the SPE when the internal parameter configurations are taken as ASYMMETRIC, ASYMMETRIC2, RANDOM, SYMMETRIC AND CLOSE, and SYMMETRIC AND NOT CLOSE. Same as the EQUAL configuration, we find that the results forecasted by FM and the actual MLEs are in good agreement.

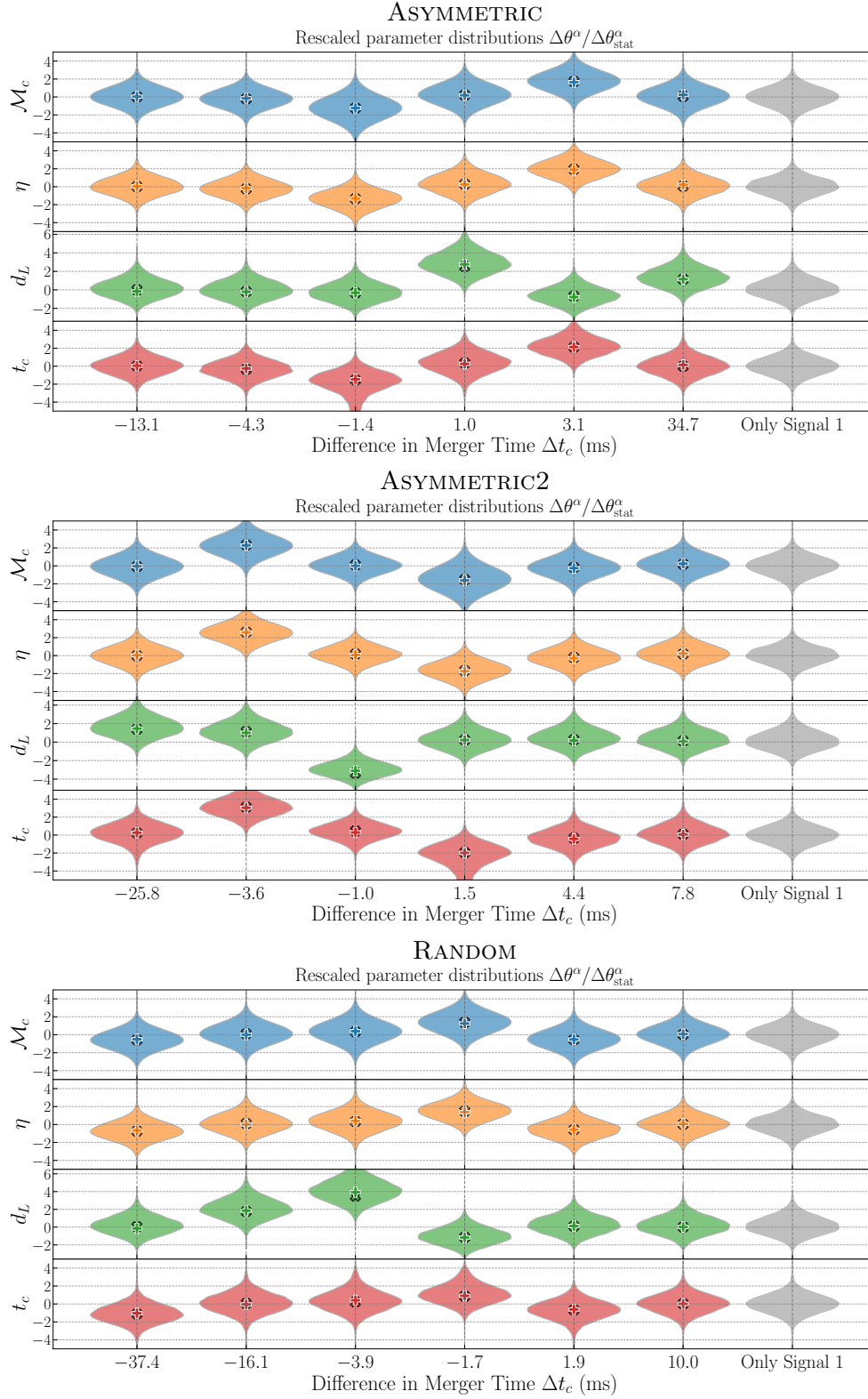


Figure D1: Same as Fig. 7, but for other parameter configurations. The configuration names are marked on the top.

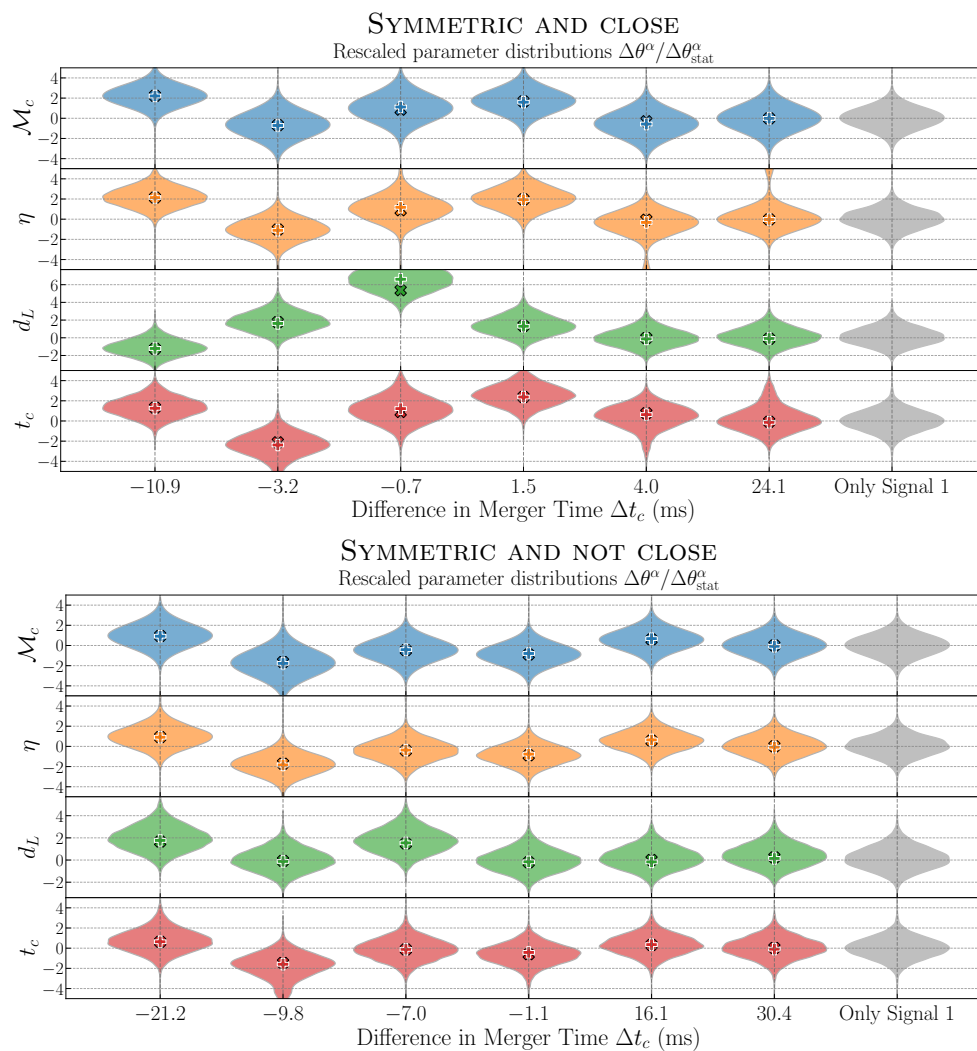


FIG D1 (continued).

References

- [1] B. P. Abbott *et al.* “GWTC-1: A Gravitational-Wave Transient Catalog of Compact Binary Mergers Observed by LIGO and Virgo during the First and Second Observing Runs”. In: *Phys. Rev. X* 9.3 (2019), p. 031040. DOI: [10.1103/PhysRevX.9.031040](https://doi.org/10.1103/PhysRevX.9.031040).
- [2] B. P. Abbott *et al.* “Observation of Gravitational Waves from a Binary Black Hole Merger”. In: *Phys. Rev. Lett.* 116.6 (2016), p. 061102. DOI: [10.1103/PhysRevLett.116.061102](https://doi.org/10.1103/PhysRevLett.116.061102).
- [3] R. Abbott *et al.* “GWTC-2: Compact Binary Coalescences Observed by LIGO and Virgo During the First Half of the Third Observing Run”. In: *Phys. Rev. X* 11 (2021), p. 021053. DOI: [10.1103/PhysRevX.11.021053](https://doi.org/10.1103/PhysRevX.11.021053).
- [4] R. Abbott *et al.* “GWTC-3: Compact Binary Coalescences Observed by LIGO and Virgo during the Second Part of the Third Observing Run”. In: *Phys. Rev. X* 13.4 (2023), p. 041039. DOI: [10.1103/PhysRevX.13.041039](https://doi.org/10.1103/PhysRevX.13.041039).
- [5] Pau Amaro-Seoane *et al.* “Laser Interferometer Space Antenna”. In: *e-prints*, arXiv:1702.00786 (Feb. 2017). DOI: [10.48550/arXiv.1702.00786](https://doi.org/10.48550/arXiv.1702.00786).
- [6] Andrea Antonelli, Ollie Burke, and Jonathan R. Gair. “Noisy neighbours: inference biases from overlapping gravitational-wave signals”. In: *Mon. Not. Roy. Astron. Soc.* 507.4 (2021), pp. 5069–5086. DOI: [10.1093/mnras/stab2358](https://doi.org/10.1093/mnras/stab2358).
- [7] Gregory Ashton *et al.* “BILBY: A user-friendly Bayesian inference library for gravitational-wave astronomy”. In: *Astrophys. J. Suppl.* 241.2 (2019), p. 27. DOI: [10.3847/1538-4365/ab06fc](https://doi.org/10.3847/1538-4365/ab06fc).
- [8] Emanuele Berti, Alessandra Buonanno, and Clifford M. Will. “Estimating spinning binary parameters and testing alternative theories of gravity with LISA”. In: *Phys. Rev. D* 71 (2005), p. 084025. DOI: [10.1103/PhysRevD.71.084025](https://doi.org/10.1103/PhysRevD.71.084025).
- [9] Johannes Buchner. “A statistical test for Nested Sampling algorithms”. In: *Statistics and Computing* 26.1-2 (2016), pp. 383–392. DOI: [10.1007/s11222-014-9512-y](https://doi.org/10.1007/s11222-014-9512-y).
- [10] Johannes Buchner. “Collaborative Nested Sampling: Big Data versus Complex Physical Models”. In: *Publ. Astron. Soc. Pac.* 131.1004 (Oct. 2019), p. 108005. DOI: [10.1088/1538-3873/aae7fc](https://doi.org/10.1088/1538-3873/aae7fc).
- [11] Johannes Buchner. “Nested sampling methods”. In: *Statist. Surv.* 17 (Jan. 2023), p. 169. DOI: [10.1214/23-ss144](https://doi.org/10.1214/23-ss144).
- [12] Alessandra Buonanno *et al.* “Comparison of post-Newtonian templates for compact binary inspiral signals in gravitational-wave detectors”. In: *Phys. Rev. D* 80 (2009), p. 084043. DOI: [10.1103/PhysRevD.80.084043](https://doi.org/10.1103/PhysRevD.80.084043).
- [13] George Casella and Roger L Berger. *Statistical inference*. Cengage Learning, 2021.

- [14] Nelson Christensen and Renate Meyer. “Markov chain Monte Carlo methods for Bayesian gravitational radiation data analysis”. In: *Phys. Rev. D* 58 (1998), p. 082001. DOI: [10.1103/PhysRevD.58.082001](https://doi.org/10.1103/PhysRevD.58.082001).
- [15] Nelson Christensen *et al.* “A Metropolis-Hastings algorithm for extracting periodic gravitational wave signals from laser interferometric detector data”. In: *Phys. Rev. D* 70 (2004), p. 022001. DOI: [10.1103/PhysRevD.70.022001](https://doi.org/10.1103/PhysRevD.70.022001).
- [16] Curt Cutler. “Angular resolution of the LISA gravitational wave detector”. In: *Phys. Rev. D* 57 (1998), pp. 7089–7102. DOI: [10.1103/PhysRevD.57.7089](https://doi.org/10.1103/PhysRevD.57.7089).
- [17] Yixuan Dang *et al.* “Impact of overlapping signals on parameterized post-Newtonian coefficients in tests of gravity”. In: *arXiv e-prints*, arXiv:2311.16184 (Nov. 2023), arXiv:2311.16184. DOI: [10.48550/arXiv.2311.16184](https://doi.org/10.48550/arXiv.2311.16184).
- [18] Lee S. Finn. “Detection, measurement and gravitational radiation”. In: *Phys. Rev. D* 46 (1992), pp. 5236–5249. DOI: [10.1103/PhysRevD.46.5236](https://doi.org/10.1103/PhysRevD.46.5236).
- [19] Sudarshan Ghonge *et al.* “Characterizing the efficacy of methods to subtract terrestrial transient noise near gravitational wave events and the effects on parameter estimation”. In: *arXiv e-prints*, arXiv:2311.09159 (Nov. 2023), arXiv:2311.09159. DOI: [10.48550/arXiv.2311.09159](https://doi.org/10.48550/arXiv.2311.09159).
- [20] Yungui Gong, Jun Luo, and Bin Wang. “Concepts and status of Chinese space gravitational wave detection projects”. In: *Nature Astron.* 5.9 (2021), pp. 881–889. DOI: [10.1038/s41550-021-01480-3](https://doi.org/10.1038/s41550-021-01480-3).
- [21] S. Hild *et al.* “Sensitivity Studies for Third-Generation Gravitational Wave Observatories”. In: *Class. Quant. Grav.* 28 (2011), p. 094013. DOI: [10.1088/0264-9381/28/9/094013](https://doi.org/10.1088/0264-9381/28/9/094013).
- [22] Yoshiaki Himemoto, Atsushi Nishizawa, and Atsushi Taruya. “Impacts of overlapping gravitational-wave signals on the parameter estimation: Toward the search for cosmological backgrounds”. In: *Phys. Rev. D* 104.4 (2021), p. 044010. DOI: [10.1103/PhysRevD.104.044010](https://doi.org/10.1103/PhysRevD.104.044010).
- [23] Qian Hu and John Veitch. “Accumulating Errors in Tests of General Relativity with Gravitational Waves: Overlapping Signals and Inaccurate Waveforms”. In: *Astrophys. J.* 945.2 (2023), p. 103. DOI: [10.3847/1538-4357/acbc18](https://doi.org/10.3847/1538-4357/acbc18).
- [24] Wen-Rui Hu and Yue-Liang Wu. “The Taiji Program in Space for gravitational wave physics and the nature of gravity”. In: *Natl. Sci. Rev.* 4.5 (2017), pp. 685–686. DOI: [10.1093/nsr/nwx116](https://doi.org/10.1093/nsr/nwx116).
- [25] Sascha Husa *et al.* “Frequency-domain gravitational waves from nonprecessing black-hole binaries. I. New numerical waveforms and anatomy of the signal”. In: *Phys. Rev. D* 93.4 (2016), p. 044006. DOI: [10.1103/PhysRevD.93.044006](https://doi.org/10.1103/PhysRevD.93.044006).
- [26] Soichiro Isoyama, Hiroyuki Nakano, and Takashi Nakamura. “Multiband Gravitational-Wave Astronomy: Observing binary inspirals with a decihertz detector, B-DECIGO”. In: *Prog. Theor. Exp. Phys.* 2018.7 (2018), 073E01. DOI: [10.1093/ptep/pty078](https://doi.org/10.1093/ptep/pty078).

- [27] Justin Janquart *et al.* “Parameter estimation methods for analyzing overlapping gravitational wave signals in the third-generation detector era”. In: *e-prints*, arXiv:2211.01304 (Nov. 2022). DOI: [10.48550/arXiv.2211.01304](https://doi.org/10.48550/arXiv.2211.01304).
- [28] Vicky Kalogera *et al.* “The Next Generation Global Gravitational Wave Observatory: The Science Book”. In: *e-prints*, arXiv:2111.06990 (Nov. 2021). DOI: [10.48550/arXiv.2111.06990](https://doi.org/10.48550/arXiv.2111.06990).
- [29] Steven M Kay. *Statistical signal processing: estimation theory*. 1993.
- [30] Sebastian Khan *et al.* “Frequency-domain gravitational waves from nonprecessing black-hole binaries. II. A phenomenological model for the advanced detector era”. In: *Phys. Rev. D* 93.4 (2016), p. 044007. DOI: [10.1103/PhysRevD.93.044007](https://doi.org/10.1103/PhysRevD.93.044007).
- [31] Chang Liu and Lijing Shao. “Neutron Star–Neutron Star and Neutron Star–Black Hole Mergers: Multiband Observations and Early Warnings”. In: *Astrophys. J.* 926.2 (2022), p. 158. DOI: [10.3847/1538-4357/ac3cbf](https://doi.org/10.3847/1538-4357/ac3cbf).
- [32] Jun Luo *et al.* “TianQin: a space-borne gravitational wave detector”. In: *Class. Quant. Grav.* 33.3 (2016), p. 035010. DOI: [10.1088/0264-9381/33/3/035010](https://doi.org/10.1088/0264-9381/33/3/035010).
- [33] Samaya Nissanke *et al.* “Exploring short gamma-ray bursts as gravitational-wave standard sirens”. In: *Astrophys. J.* 725 (2010), pp. 496–514. DOI: [10.1088/0004-637X/725/1/496](https://doi.org/10.1088/0004-637X/725/1/496).
- [34] Elia Pizzati *et al.* “Toward inference of overlapping gravitational-wave signals”. In: *Phys. Rev. D* 105.10 (2022), p. 104016. DOI: [10.1103/PhysRevD.105.104016](https://doi.org/10.1103/PhysRevD.105.104016).
- [35] Tania Regimbau and Scott A. Hughes. “Gravitational-wave confusion background from cosmological compact binaries: Implications for future terrestrial detectors”. In: *Phys. Rev. D* 79 (2009), p. 062002. DOI: [10.1103/PhysRevD.79.062002](https://doi.org/10.1103/PhysRevD.79.062002).
- [36] David Reitze *et al.* “Cosmic Explorer: The U.S. Contribution to Gravitational-Wave Astronomy beyond LIGO”. In: *Bull. Am. Astron. Soc.* 51.7 (2019), p. 035. DOI: [10.48550/arXiv.1907.04833](https://doi.org/10.48550/arXiv.1907.04833).
- [37] David Reitze *et al.* “The US Program in Ground-Based Gravitational Wave Science: Contribution from the LIGO Laboratory”. In: *Bull. Am. Astron. Soc.* 51 (Mar. 2019), p. 141. DOI: [10.48550/arXiv.1903.04615](https://doi.org/10.48550/arXiv.1903.04615).
- [38] Philip Reilton and Vivien Raymond. “Parameter estimation bias from overlapping binary black hole events in second generation interferometers”. In: *Phys. Rev. D* 104.8 (2021), p. 084039. DOI: [10.1103/PhysRevD.104.084039](https://doi.org/10.1103/PhysRevD.104.084039).
- [39] I. M. Romero-Shaw *et al.* “Bayesian inference for compact binary coalescences with bilby: validation and application to the first LIGO–Virgo gravitational-wave transient catalogue”. In: *Mon. Not. Roy. Astron. Soc.* 499.3 (2020), pp. 3295–3319. DOI: [10.1093/mnras/staa2850](https://doi.org/10.1093/mnras/staa2850).
- [40] Anuradha Samajdar *et al.* “Biases in parameter estimation from overlapping gravitational-wave signals in the third-generation detector era”. In: *Phys. Rev. D* 104.4 (2021), p. 044003. DOI: [10.1103/PhysRevD.104.044003](https://doi.org/10.1103/PhysRevD.104.044003).

- [41] B. Sathyaprakash *et al.* “Scientific Objectives of Einstein Telescope”. In: *Class. Quant. Grav.* 29 (2012). Ed. by Mark Hannam *et al.* [Erratum: *Class.Quant.Grav.* 30, 079501 (2013)], p. 124013. DOI: [10.1088/0264-9381/29/12/124013](https://doi.org/10.1088/0264-9381/29/12/124013).
- [42] Sanjib Sharma. “Markov Chain Monte Carlo Methods for Bayesian Data Analysis in Astronomy”. In: *Ann. Rev. Astron. Astrophys.* 55 (2017), pp. 213–259. DOI: [10.1146/annurev-astro-082214-122339](https://doi.org/10.1146/annurev-astro-082214-122339).
- [43] Kevin J. Shuman and Neil J. Cornish. “Massive black hole binaries and where to find them with dual detector networks”. In: *Phys. Rev. D* 105.6 (2022), p. 064055. DOI: [10.1103/PhysRevD.105.064055](https://doi.org/10.1103/PhysRevD.105.064055).
- [44] John Skilling. “Nested Sampling”. In: *Bayesian Inference and Maximum Entropy Methods in Science and Engineering*. Vol. 735. American Institute of Physics Conference Series. Nov. 2004, p. 395. DOI: [10.1063/1.1835238](https://doi.org/10.1063/1.1835238).
- [45] John Skilling. “Nested sampling for general Bayesian computation”. In: *Bayesian Analysis* 1.4 (2006), pp. 833–859. DOI: [10.1214/06-BA127](https://doi.org/10.1214/06-BA127).
- [46] Rory Smith *et al.* “Bayesian Inference for Gravitational Waves from Binary Neutron Star Mergers in Third Generation Observatories”. In: *Phys. Rev. Lett.* 127.8 (2021), p. 081102. DOI: [10.1103/PhysRevLett.127.081102](https://doi.org/10.1103/PhysRevLett.127.081102).
- [47] Rory J. E. Smith *et al.* “Massively parallel Bayesian inference for transient gravitational-wave astronomy”. In: *Mon. Not. Roy. Astron. Soc.* 498.3 (2020), pp. 4492–4502. DOI: [10.1093/mnras/staa2483](https://doi.org/10.1093/mnras/staa2483).
- [48] Michele Vallisneri. “Use and abuse of the Fisher information matrix in the assessment of gravitational-wave parameter-estimation prospects”. In: *Phys. Rev. D* 77 (2008), p. 042001. DOI: [10.1103/PhysRevD.77.042001](https://doi.org/10.1103/PhysRevD.77.042001).
- [49] Ziming Wang *et al.* “Extending the Fisher Information Matrix in Gravitational-wave Data Analysis”. In: *Astrophys. J.* 932 (Mar. 2022), p. 102. DOI: [10.3847/1538-4357/ac6b99](https://doi.org/10.3847/1538-4357/ac6b99).
- [50] Ziming Wang *et al.* “Simultaneous bounds on the gravitational dipole radiation and varying gravitational constant from compact binary inspirals”. In: *Phys. Lett. B* 834 (2022), p. 137416. DOI: [10.1016/j.physletb.2022.137416](https://doi.org/10.1016/j.physletb.2022.137416).
- [51] Junjie Zhao *et al.* “Probing dipole radiation from binary neutron stars with ground-based laser-interferometer and atom-interferometer gravitational-wave observatories”. In: *Phys. Rev. D* 104.8 (2021), p. 084008. DOI: [10.1103/PhysRevD.104.084008](https://doi.org/10.1103/PhysRevD.104.084008).